

## **Supporting Information**

### **Tailored on-surface fabrication of mesoporous metallic composites by direct pyrolysis of metal ion-accumulated micellar films for enhanced electrocatalytic water splitting**

Jingchun Wang, Yan Sun, Yan Cui, and Huibin Qiu

## Experimental

### Chemicals and materials

Ruthenium (III) chloride hydrate ( $\text{RuCl}_3 \cdot x\text{H}_2\text{O}$ , 98%), platinum (II) nitrate ( $\text{Pt}(\text{NO}_3)_2$ , 98%), iridous (III) chloride ( $\text{IrCl}_3$ , 99.9%), palladium(II) chloride ( $\text{PdCl}_2$ , 99%), ferric chloride (III) hydrate ( $\text{FeCl}_3 \cdot 6\text{H}_2\text{O}$ , 99.9%) and other reagents were purchased from Sigma-Aldrich. All raw reagents were purchased from regular commercial platform and used without any further purification. Nickel foam was sonicated in a solution of hydrochloric acid for 15 min to remove the oxides on the surface, and subsequently rinsed with water, acetone and ethanol. Carbon cloth was sonicated in acetone and rinsed with water and ethanol to remove the surface-adsorbed components, and then dried naturally. All other manipulations were operated under an open atmosphere unless otherwise stated.  $\text{PS}_{480}\text{-}b\text{-P2VP}_{490}$  (the subscripts denote the degree of polymerization of the corresponding block) block copolymer was synthesized by sequential anionic polymerization in an inert atmosphere according to the previously reported method.<sup>1</sup>

### Preparation of mesoporous composite film with spherical cavities on desired substrates

Typically, 100  $\mu\text{L}$  of a solution of  $\text{PS}_{480}\text{-}b\text{-P2VP}_{490}$  (10 mg/mL in tetrahydrofuran, fully dissolved as unimers) was uniformly coated on a desired substrate (e.g. nickel foam, carbon cloth, silicon wafer and carbon film-coated copper grid; area:  $\sim 1 \text{ cm}^2$ ; treated by plasma in advance). Then, the decorated substrate was immersed in a solution of  $\text{RuCl}_3$  or  $\text{Pt}(\text{NO}_3)_2$  or  $\text{IrCl}_3$  or  $\text{PdCl}_2$  or  $\text{FeCl}_3$  (0.10 mmol of precursor in 1 mL of ethanol). After 3 h, the resulting sample was dried under a gentle stream of nitrogen, followed by pyrolyzed at 300, 350, 400, 450, and 600  $^\circ\text{C}$  for 4 h in air.

### Preparation of mesoporous composite film with cylindrical cavities on nickel foam

Typically, the nickel foam decorated with the spherical micelle film and accumulated metal ions was immersed in *n*-hexane for 1 h. Subsequently, the obtained sample was pyrolyzed at 300  $^\circ\text{C}$  for 4 h.

### Characterization

Transmission electron microscopy (TEM) micrographs were acquired on a Thermo Scientific Talos L120C G2 microscope with an electron acceleration voltage of 120 kV. High-resolution TEM (HRTEM) micrographs, high-angle annular dark-field STEM S58 (HAADF-STEM) micrographs and corresponding energy dispersive X-ray spectroscopy (EDS) elemental

mapping micrographs were acquired on a Thermo Scientific Talos F200X microscope with an electron acceleration voltage of 200 kV. The sample was peeled from the substrates by sonication, dispersing in ethanol, and dropping onto a carbon film-coated copper grid for the tests. Scanning electron microscopy (SEM) micrographs were acquired on a JEOL 48 JSM7800F Prime microscope and a TESCAN MAIA3 microscope with an electron acceleration voltage of 5.0 kV. Before SEM characterization, the samples were coated with a thin layer of Pt for better observation. X-ray diffraction (XRD) patterns were recorded on a Japan Rigaku Mini Flex 600 diffractometer equipped with Cu K $\alpha$  radiation (40 kV, 40 mA). X-ray photoelectron spectroscopy (XPS) was conducted on a Kratos AXIS UltraDLD instrument using Al K $\alpha$  radiation (1486 eV). Nitrogen sorption measurements were analyzed on a Micromeritics ASAP 2050 instrument. ICP-MS data were collected on Agilent 7850 system. Thermogravimetric analysis (TGA) was measured on a Netzsch STA449C thermal analyzer with a heating rate of 10 °C min<sup>-1</sup> and a flow rate of 50 mL min<sup>-1</sup> under air atmosphere. Contact angles were measured by a Lauda Scientific LSA100 system equipped with a high-speed camera at room temperature.

### **Electrochemical Measurements**

All electrochemical measurements were performed on a CH Instrument (Chenhua CHI760E) electrochemistry workstation with an impedance module. Oxygen evolution reaction (OER) and hydrogen evolution reaction (HER) were evaluated in a standard three-electrode system in 1.0 M KOH by using the as-prepared sample, Ag/AgCl (3.0 M KCl) and graphite rod as the working electrode, reference electrode and counter electrode, respectively. Overall water splitting measurements were performed with a two-electrode system by using as-the prepared sample as both anode and cathode in 1.0 M KOH at room temperature. Linear sweep voltammetry (LSV) curves were collected with a scan rate of 5 mV s<sup>-1</sup> with 90% iR- correction ( $E_{iR\text{-corrected}} = E_{\text{original}} - 90\% \times I \times iR_s$ ). Chronoamperometric tests were recorded at room temperature. Electrochemical impedance spectroscopy (EIS) measurements were performed at a fixed overpotential of 200 mV for OER with a frequency range of 0.01 Hz to 100 kHz (10 mV amplitude). The  $C_{dl}$  values were confirmed from the cyclic voltammogram (CV) in the double layer region (without faradaic processes) at different scan rates. All the measured potentials were calibrated with respect to the reversible hydrogen electrode (RHE) according to the following conversion:  $E_{\text{RHE}} = E_{\text{Ag/AgCl}} + E_{\text{Ag/AgCl}}^0 + 0.059 \times \text{pH}$ . Tafel

plots were calculated with the linear portions at a low overpotential fitted to the Tafel equation ( $\eta = b \times \log j + a$ , where  $\eta$  is overpotential,  $j$  is the current density, and  $b$  is the Tafel slope).

### Load Calculations

The ratio of Ru and pyridyl group in the  $\text{Ru}^{3+}$ -accumulated micellar film was approximately 1 : 4, which was calculated as:

$$\frac{n_{\text{Ru}}}{n_{\text{P2VP}}} = \frac{m_{\text{Ru}}/M_{\text{Ru}}}{N_{\text{P2VP}} \times m_{\text{PS-}b\text{-P2VP}}/M_{\text{PS-}b\text{-P2VP}}}$$

where:  $n_{\text{Ru}}$  is molar mass of Ru;  $m_{\text{Ru}}$  is mass of Ru (mass of Ru was determined by ICP-MS analysis);  $M_{\text{Ru}}$  is relative atomic mass of Ru;  $n_{\text{P2VP}}$  is molar mass of P2VP;  $m_{\text{PS-}b\text{-P2VP}}$  is mass of PS-*b*-P2VP (mass of PS-*b*-P2VP was obtained by experimental addition);  $M_{\text{PS-}b\text{-P2VP}}$  is molecular mass of PS-*b*-P2VP (molecular mass of PS-*b*-P2VP was determined by GPC analysis);  $N_{\text{P2VP}} = 490$  (degree of polymerization of P2VP).

The area loading of mesoporous film on nickel foam, which was calculated as:

$$\text{Mass loading} = \frac{m_{\text{Ru+Ni}}}{A_{\text{nickel foam}}}$$

where:  $m_{\text{Ru+Ni}}$  is mass of Ru and Ni (mass of Ru and Ni was determined by ICP-MS and XPS analysis),  $A_{\text{nickel foam}}$  is the area of nickel foam as electrode.

### Anion-exchange membrane water electrolyzer (AEMWE) test

Anion-exchange membrane water electrolyzer (AEMWE) with serpentine flow channel was tested for practical applications in which the mesoporous composite film with cylindrical cavities on nickel foam were used as the cathode and anode plates. Anion exchange membrane (AEM) purchased from Dioxide Materials Corporation (X37-50-grade 60) were soaked in an aqueous solution of 1.0 M KOH overnight to activate the membrane before use. Mesoporous composite film with cylindrical cavities on nickel foam || AEM || mesoporous composite film with cylindrical cavities on nickel foam system was assembled for further testing. AEMWE test was performed at 80 °C with 1.0 M KOH pumped at a flow rate of 30 mL min<sup>-1</sup> by a peristaltic pump. Polarization curves were obtained at a step rate of 0.02 V over a voltage range of 1.2 to 2.1 V. Long-term stability tests were carried out at a current density of 2 A cm<sup>-2</sup> and a temperature of 80 °C (the area of nickel foam is 1 cm × 1 cm; the mass loading is 0.55 mg/cm<sup>2</sup>). Commercial IrO<sub>2</sub> and Pt/C (ca. 5 mg mL<sup>-1</sup> in ethanol; the mass loading is 0.55 mg/cm<sup>2</sup>) were

separately mixed with Nafion binder and subsequently casted on carbon cloth (the area of carbon cloth is 1 cm × 1 cm), which were used as the anode and cathode, respectively.

### **Density functional theory (DFT) calculations**

In this study, all the first-principles calculations were performed using spin-polarized DFT with the Vienna ab-initio simulation package (VASP).<sup>2</sup> Such as geometry relaxations, total electronic energy calculations and vibrational frequency calculations, all employed the generalized gradient approximation (GGA) in the Perdew-Burke-Ernzerh (PBE) format,<sup>3</sup> the projector-augmented wave (PAW)<sup>4</sup> pseudopotentials and a plane wave basis with the cut-off energy of 450 eV. The Grimme D3 correction using a coordination number dependent dispersion correction.<sup>5</sup> All the calculations are performed in the framework of the density functional theory with the projector augmented plane-wave method, as implemented in the Vienna ab initio simulation package. The generalized gradient approximation proposed by Perdew, Burke, and Ernzerhof is selected for the exchange-correlation potential. The Grimme D3 correction uses a coordination number-dependent dispersion correction.

The cut-off energy for plane wave is set to 450 eV. The energy criterion is set to  $10^{-4}$  eV in iterative solution of the Kohn-Sham equation. A vacuum layer of 15 Å is added perpendicular to the sheet to avoid artificial interaction between periodic images. The Brillouin zone integration is performed using a  $2 \times 2 \times 1$  k-mesh.<sup>6</sup> All the structures are relaxed until the residual forces on the atoms have declined to less than 0.03 eV/Å. A dipole correction was applied for all slab models. Spin polarization is included in the calculations. The Visualization for Electronic and Structural Analysis (VESTA) software<sup>7</sup> was used for visualization of the atomic structures. The construction of the DFT models involved an atomic ratio of Ru : Ni : N = 4 : 4 : 1.

The Free energy changes ( $\Delta G$ ) of reaction intermediates could be calculated by the following equation:

$$\Delta G = \Delta E + \Delta E_{ZPE} - T \times \Delta S$$

where  $\Delta E$  is the adsorption energy on the cluster surface from DFT calculations. The  $\Delta E_{ZPE}$  and  $\Delta S$  are the difference for the zero-point energy and entropy. The zero-point energy and entropy are calculated at the standard conditions corresponding to the pressure of 101325 Pa (~1 bar) of H<sub>2</sub> at a temperature of 298.15 K.

The projected densities of states (PDOS) of all structures were calculated by a Monkhorst Brillouin sampling mesh of  $8 \times 8 \times 4$ . The integral overlap region between the Ru orbital and the O orbital below the Fermi level of  $\text{H}_2\text{O-N-RuO}_2$ ,  $\text{H}_2\text{O-N-Ru/RuO}_2$ ,  $\text{H}_2\text{O-N-RuO}_2/\text{NiO}$ ,  $\text{H}_2\text{O-Ru/RuO}_2/\text{NiO}$  and  $\text{H}_2\text{O-N-Ru/RuO}_2/\text{NiO}$  were calculated by the following equation:

$$\text{Area} = \int_{E=-\infty}^{E=E_f} f_{min}(E) dE$$

where:

$$f_{min}(E) = \begin{cases} f_s(E), & \text{if } f_{water}(E) > f_s(E) \\ f_{water}(E), & \text{if } f_{water}(E) < f_s(E) \end{cases}$$

$E_f$  : Fermi level;  $f_s$  and  $f_{water}$  : PDOS of Ru orbital and the O orbital.

## Supplementary Figures

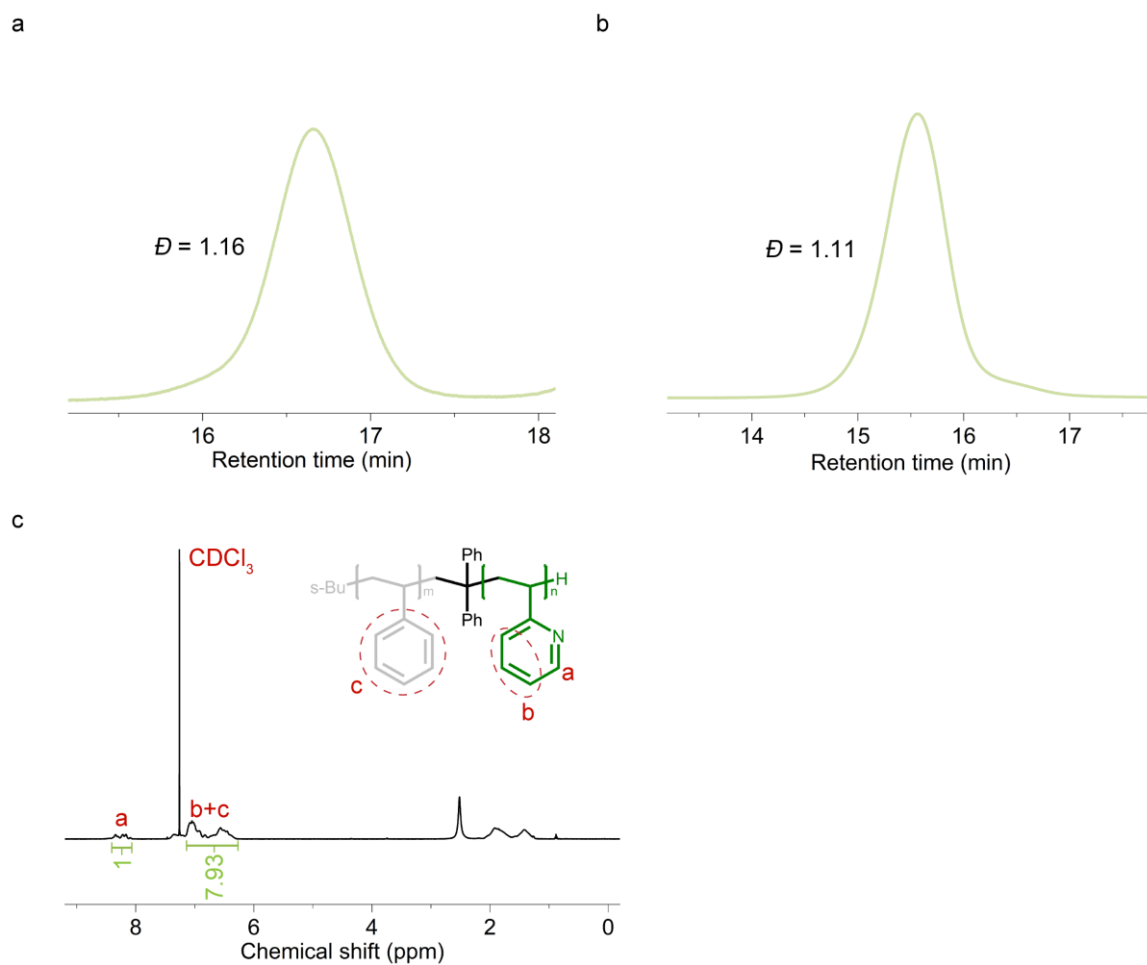


**Fig. S1.** (a) GPC trace of PS homopolymer obtained before the sequential polymerization of the P2VP block. (b) GPC trace and (c)  $^1\text{H}$  NMR spectra of the  $\text{PS}_{480}\text{-}b\text{-P2VP}_{490}$  block copolymer.

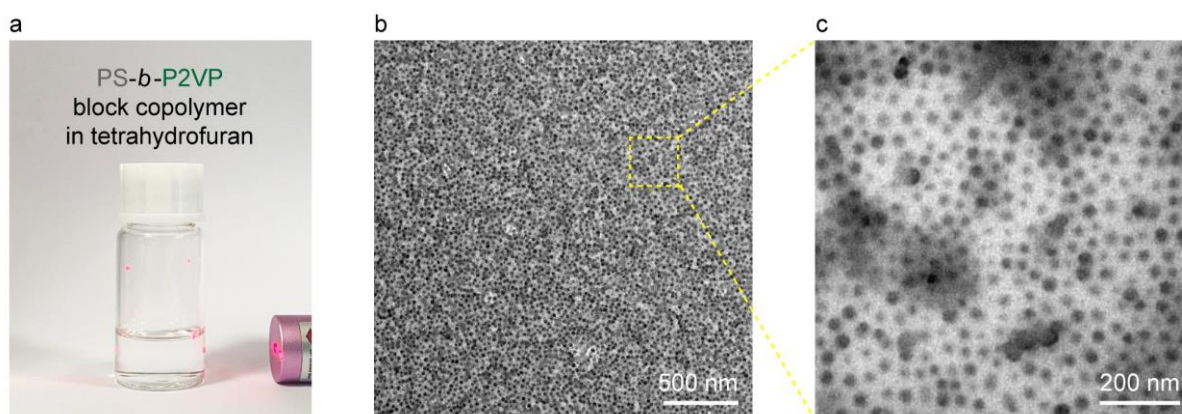


**Fig. S2.** (a) Photograph of a solution of PS<sub>480</sub>-*b*-P2VP<sub>490</sub> block copolymer in tetrahydrofuran. (b and c) TEM images of PS<sub>480</sub>-*b*-P2VP<sub>490</sub> micellar film on a carbon film-coated copper grid.

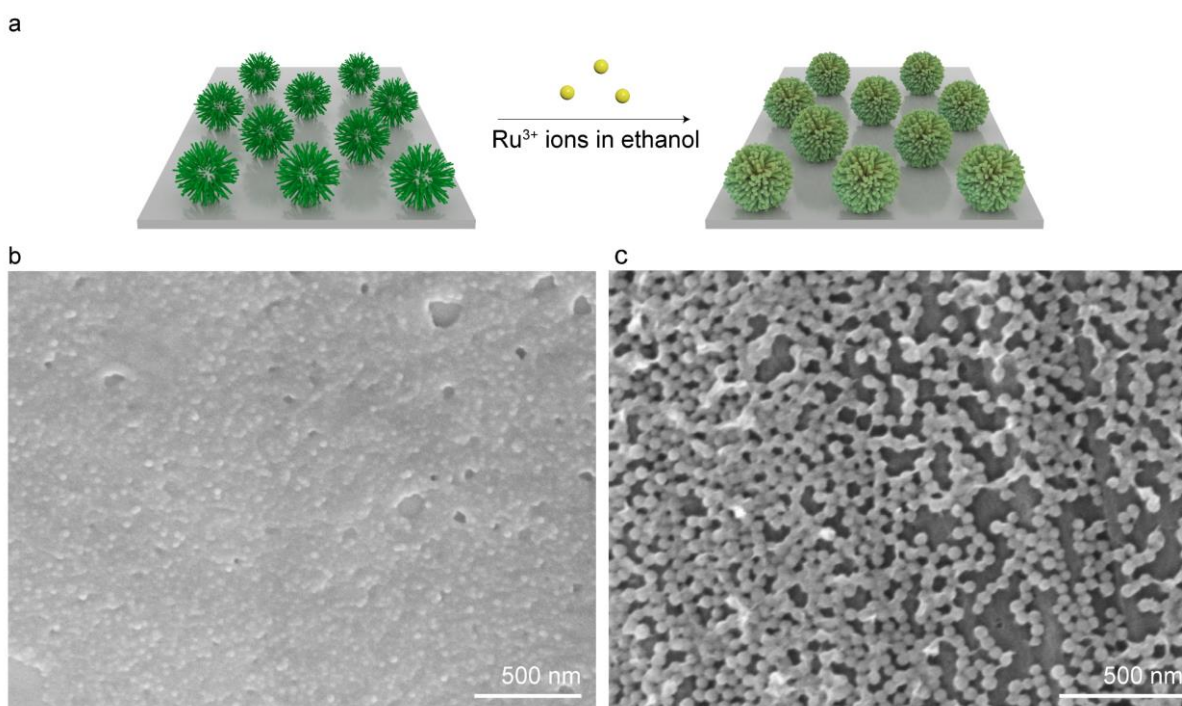


**Fig. S3.** (a) Schematic illustration for the decoration of a solution of self-assembled PS<sub>480</sub>-*b*-P2VP<sub>490</sub> spherical micelles<sup>1</sup> in methanol on a substrate and the subsequent immersion in a solution of Ru<sup>3+</sup> ions in ethanol. (b and c) SEM images of PS<sub>480</sub>-*b*-P2VP<sub>490</sub> spherical micelles and Ru<sup>3+</sup>-accumulated spherical micelles on nickel foam.

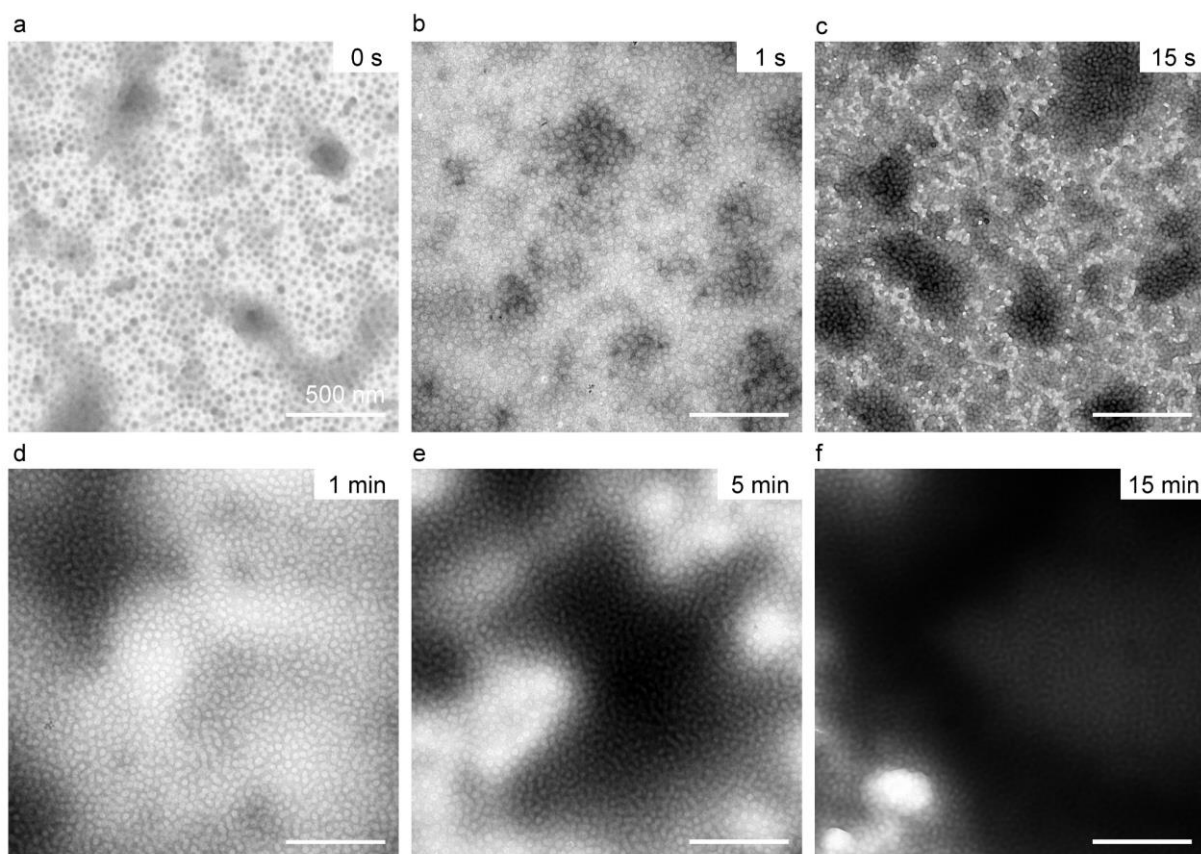


**Fig. S4.** TEM images of PS<sub>480</sub>-*b*-P2VP<sub>490</sub> micellar film on carbon film-coated copper grid (a) before and (b–f) after immersion in a solution of Ru<sup>3+</sup> ions in ethanol for (b) 1 s, (c) 15 s, (d) 1 min, (e) 5 min, and (f) 15 min.

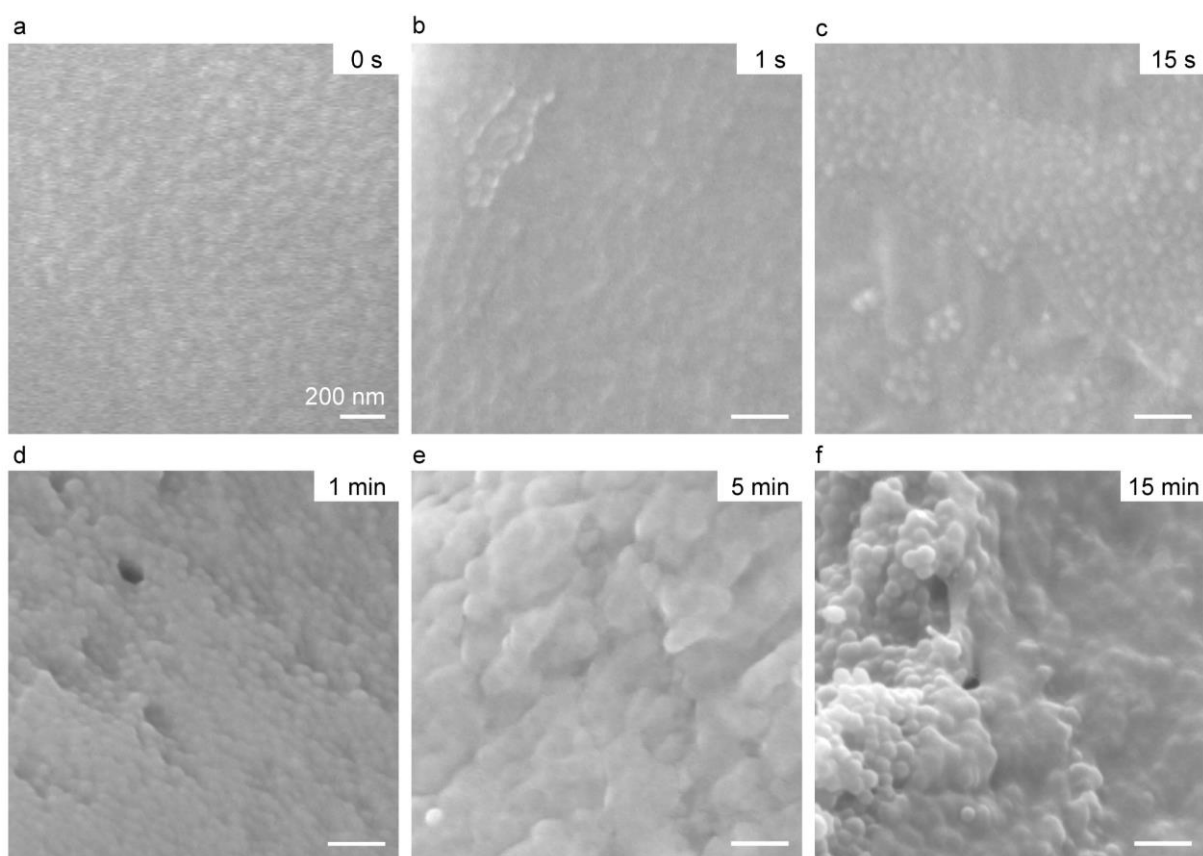


**Fig. S5.** SEM images of PS<sub>480</sub>-*b*-P2VP<sub>490</sub> micellar film on nickel foam (a) before and (b–f) after immersion in a solution of Ru<sup>3+</sup> ions in ethanol for (b) 1 s, (c) 15 s, (d) 1 min, (e) 5 min, and (f) 15 min.

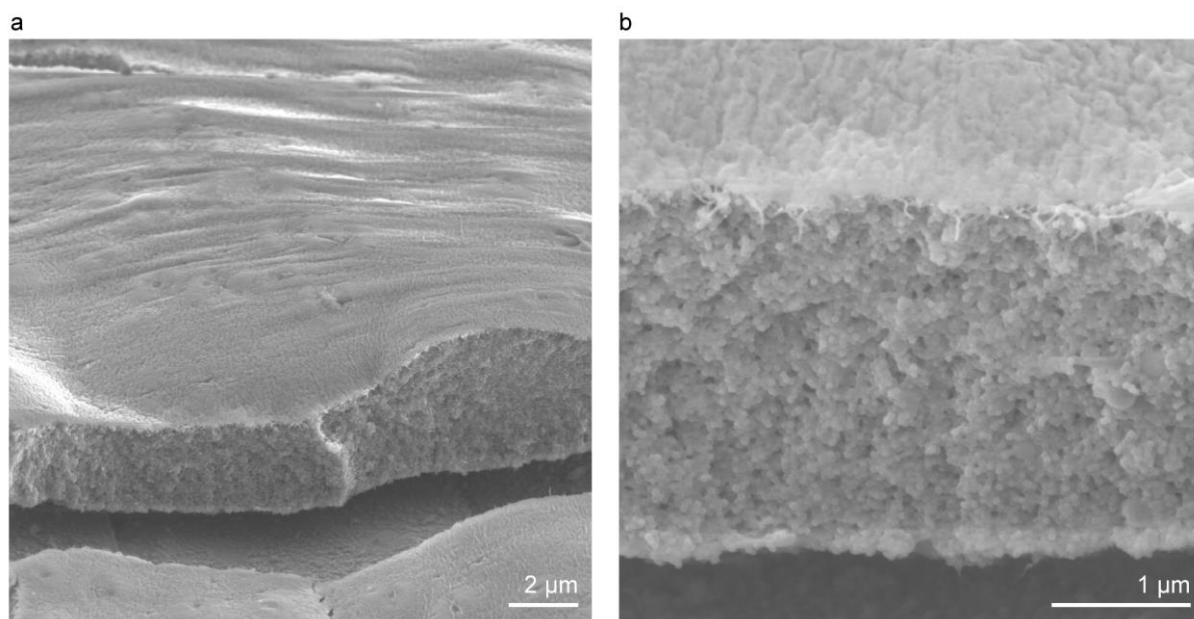


**Fig. S6.** SEM images of the cracked positions of Ru<sup>3+</sup>-accumulated spherical micelle film on nickel foam.

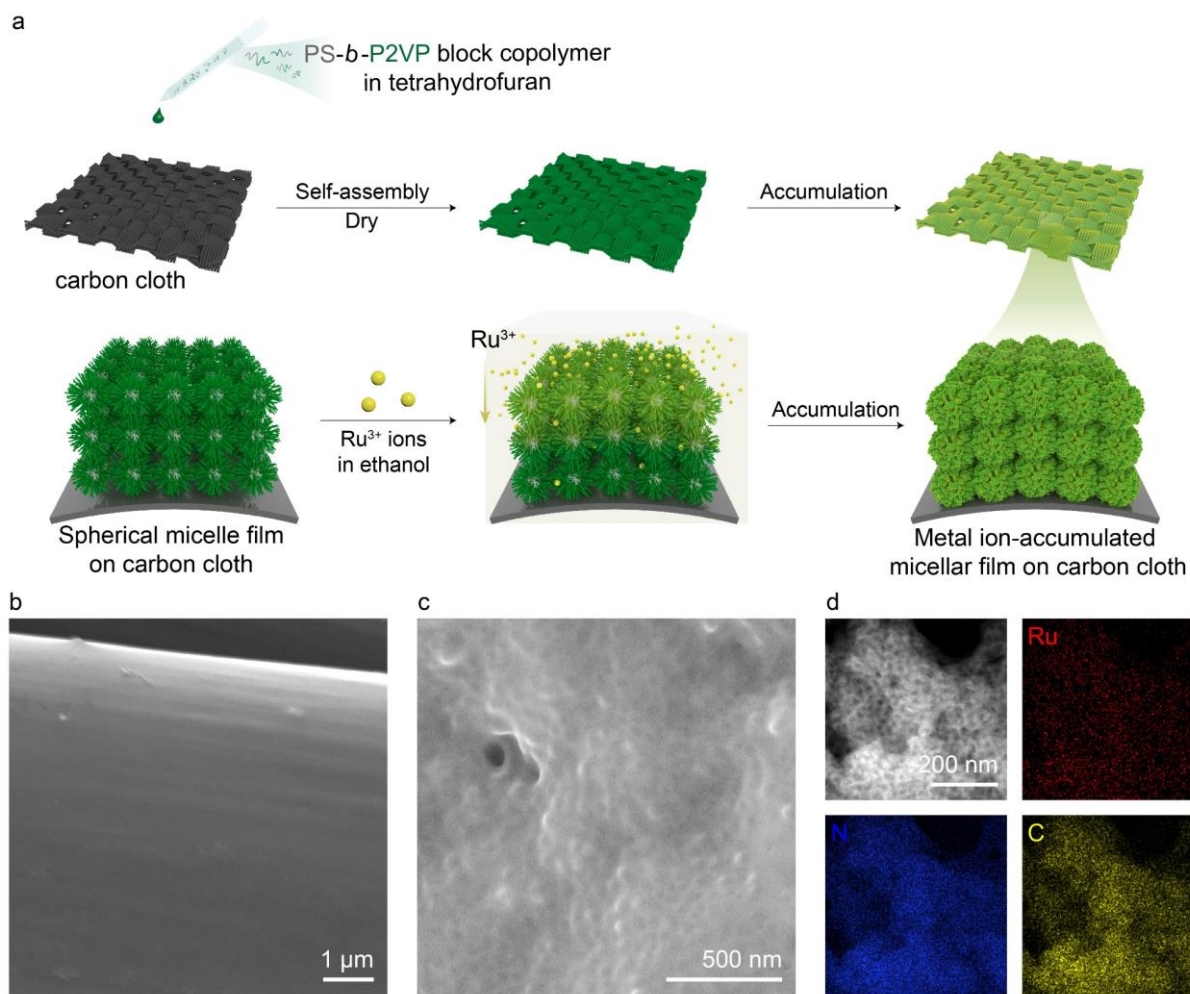


**Fig. S7.** (a) Schematic illustration of the formation of micellar film on carbon cloth and the subsequent accumulation of Ru<sup>3+</sup> ions in an ethanol solution. (b) SEM image of PS<sub>480</sub>-*b*-P2VP<sub>490</sub> micellar film on carbon cloth, (c) SEM image and (d) elemental mapping images of metal ion-accumulated PS<sub>480</sub>-*b*-P2VP<sub>490</sub> micellar film on carbon cloth. The sample was peeled from the carbon cloth by ultrasonication for the tests.

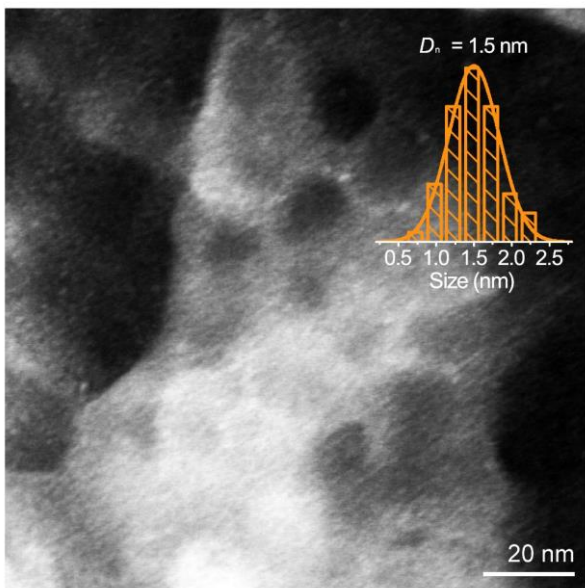


**Fig. S8.** Size distribution of Ru nanoparticles in meta ion-accumulated micellar film ( $D_n$ : number-average diameter).



**Fig. S9.** Photograph of (a) PS<sub>480</sub>-*b*-P2VP<sub>490</sub> micellar film-decorated on nickel foam and (b) bare nickel foam after immersion in a solution of Ru<sup>3+</sup> ions in ethanol for 3 h.

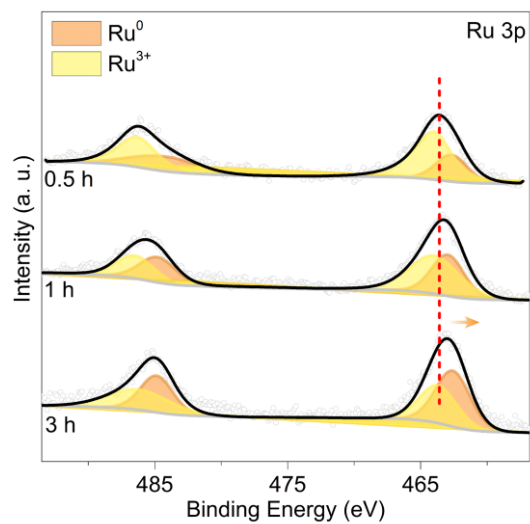


**Fig. S10.** High-resolution XPS spectra of Ru 3p and of mesoporous composite films prepared by immersing the PS<sub>480</sub>-*b*-P2VP<sub>490</sub> micellar film on nickel foam in a solution of Ru<sup>3+</sup> ion in ethanol for 0.5, 1, and 3 h.

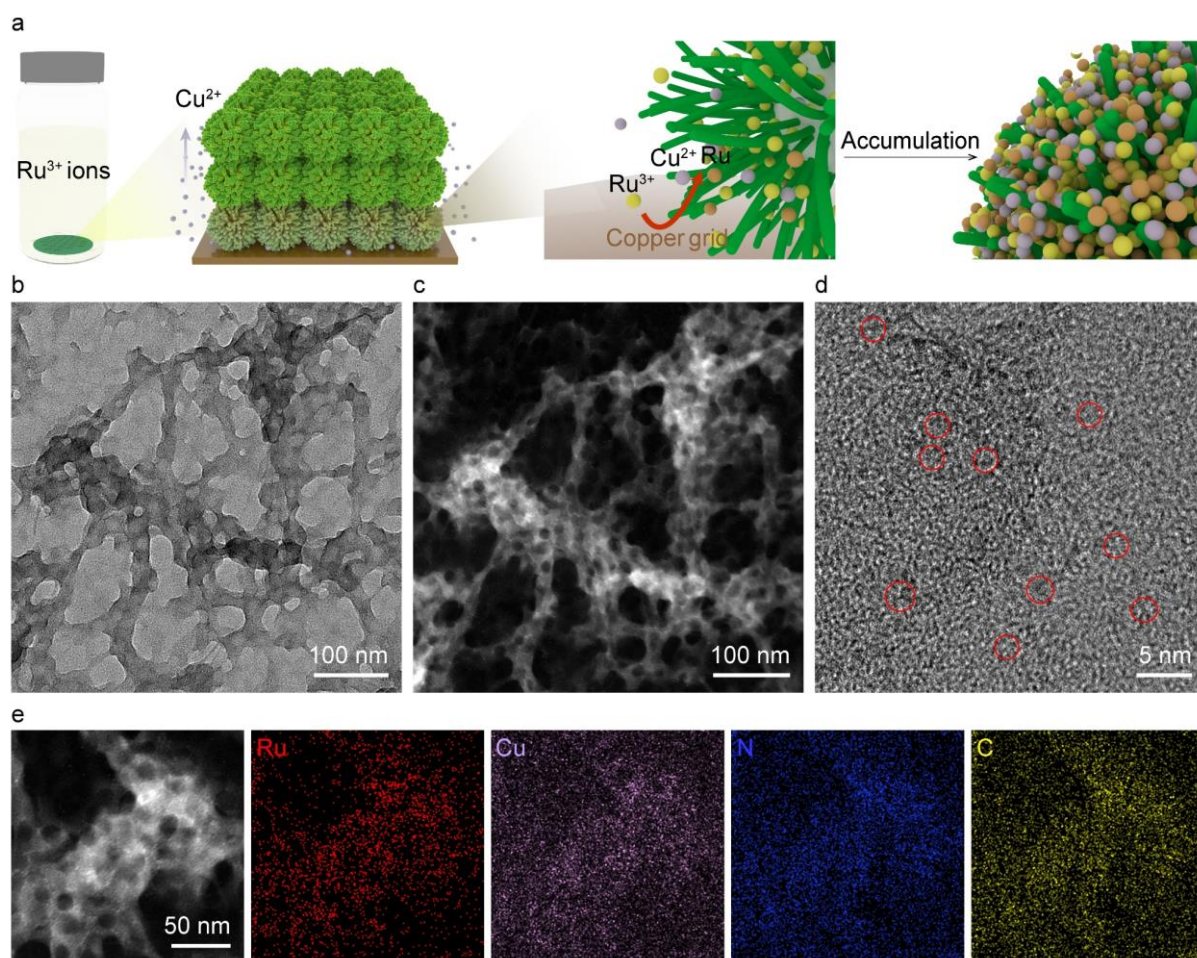


**Fig. S11.** (a) Schematic illustration of the accumulation of Ru<sup>3+</sup> ions in an ethanol solution on carbon film-coated copper grid. (b) TEM, (c) HAADF-STEM, (d) HRTEM, and (e) elemental mapping images of metal-accumulated micellar film on carbon film-coated copper grid.

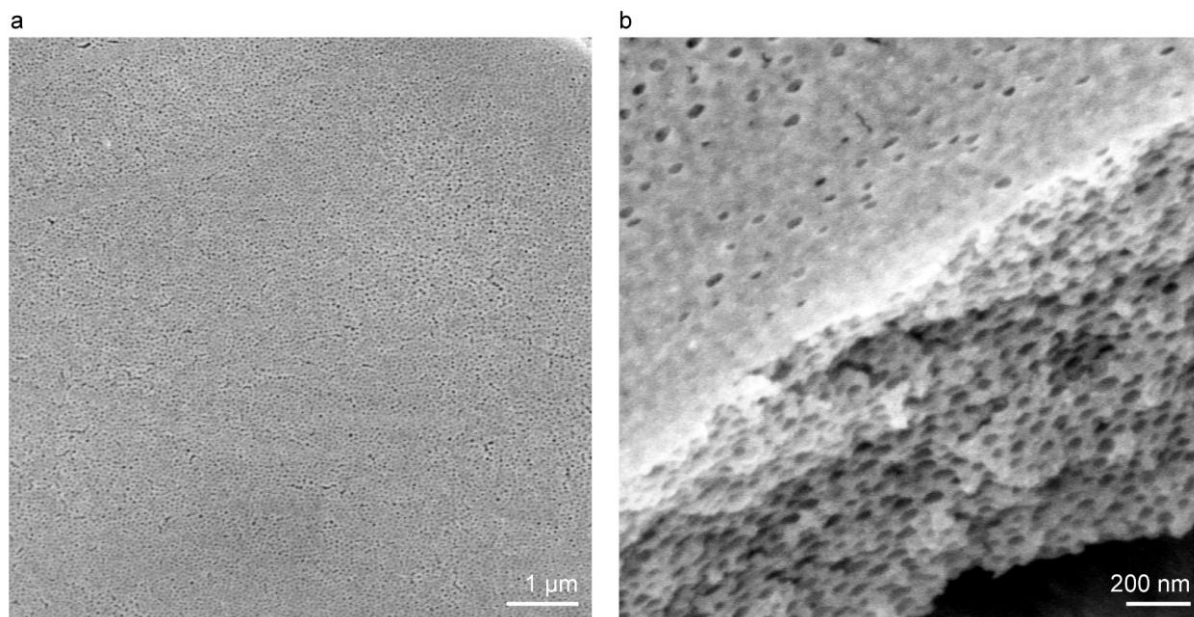


**Fig. S12.** SEM images of the (a) surface and (b) fracture of Ru<sup>3+</sup>-derived mesoporous composite film with spherical cavities on nickel foam formed after pyrolysis at 300 °C in air.

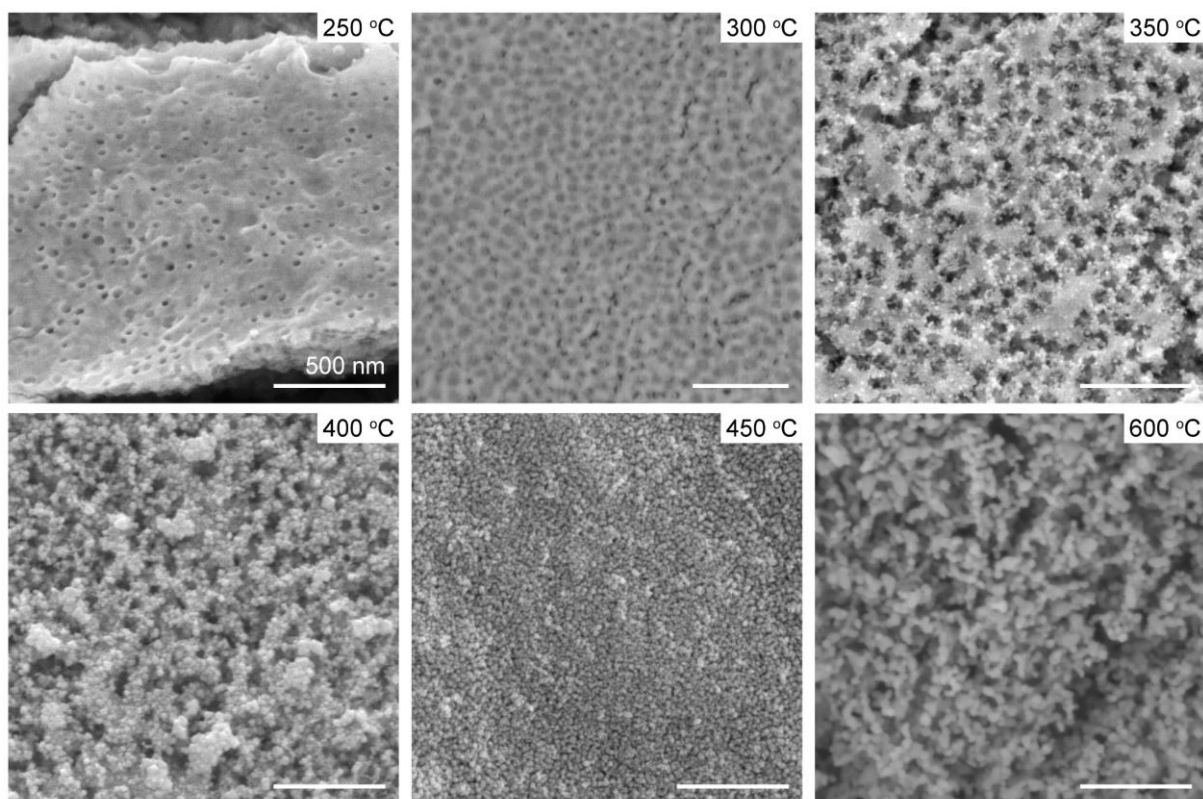


**Fig. S13.** SEM images of Ru<sup>3+</sup>-accumulated spherical micelle film after pyrolysis at 250, 300, 350, 400, 450 and 600 °C in air.

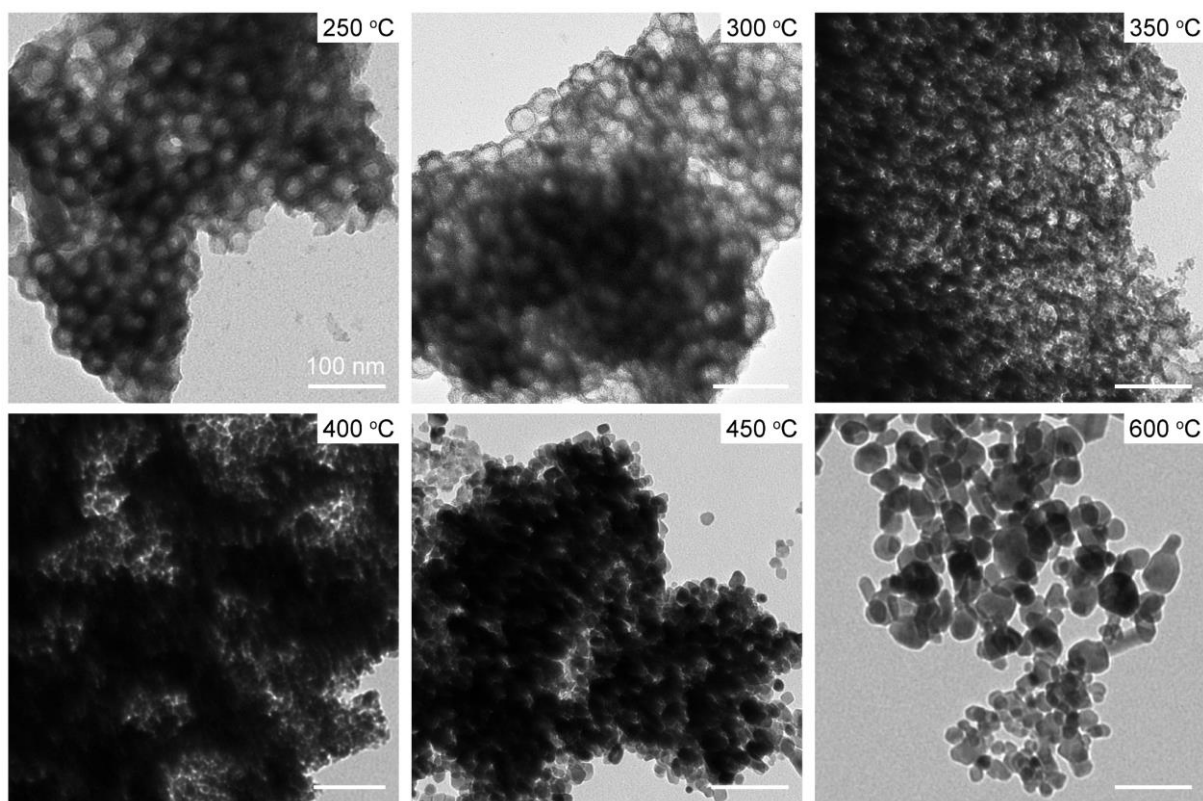


**Fig. S14.** TEM images of  $\text{Ru}^{3+}$ -accumulated spherical micelle film after pyrolysis at 250, 300, 350, 400, 450 and 600 °C in air.

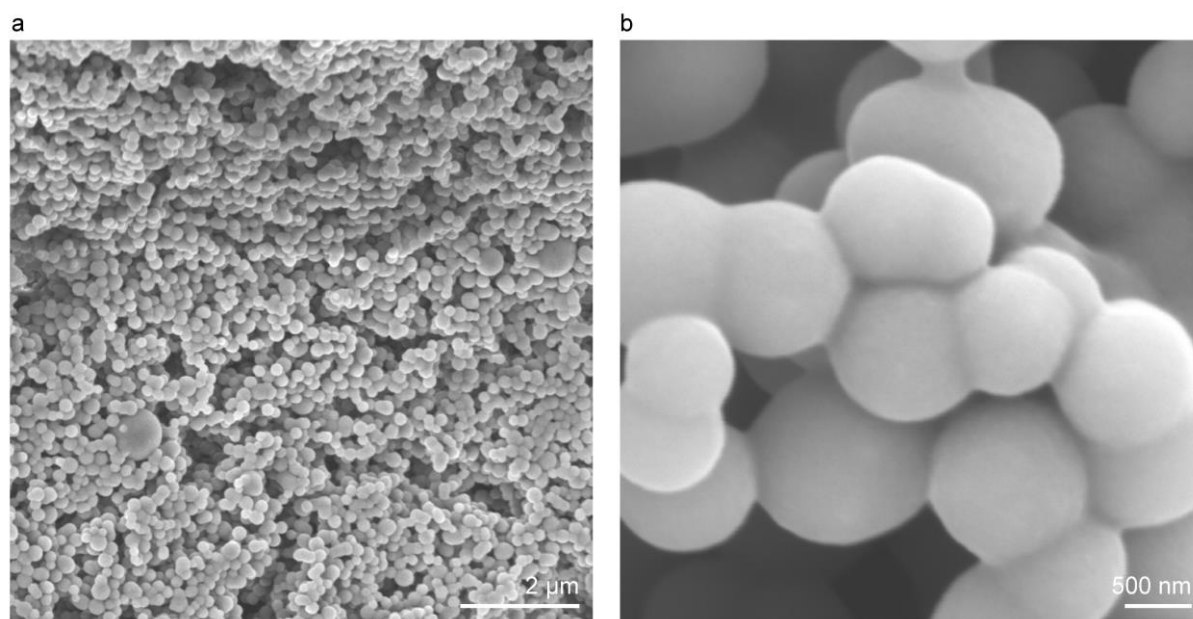


**Fig. S15.** SEM images of  $\text{PS}_{480}$ -*b*- $\text{P2VP}_{490}$  spherical micelle film on nickel foam after pyrolysis at 300 °C in air.

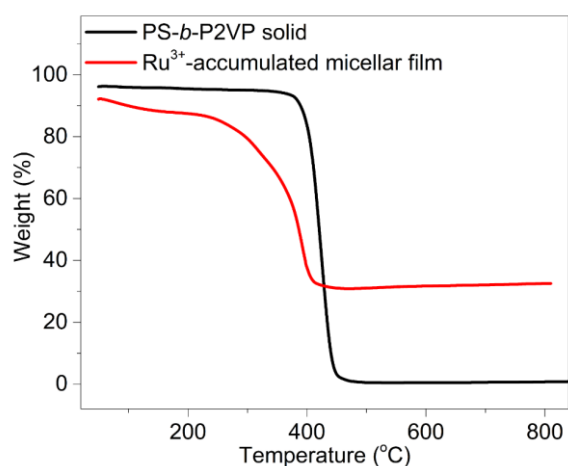


**Fig. S16.** TGA curves of PS<sub>480</sub>-*b*-P2VP<sub>490</sub> solid and Ru<sup>3+</sup>-accumulated spherical micelle film. PS-*b*-P2VP partially decomposed at 300 °C in the presence of accumulated metal species, although it was more stable in a pure state. It appears that the coordination complexes formed by PS-*b*-P2VP micelles and metal species are less thermally stable than the block copolymer itself.

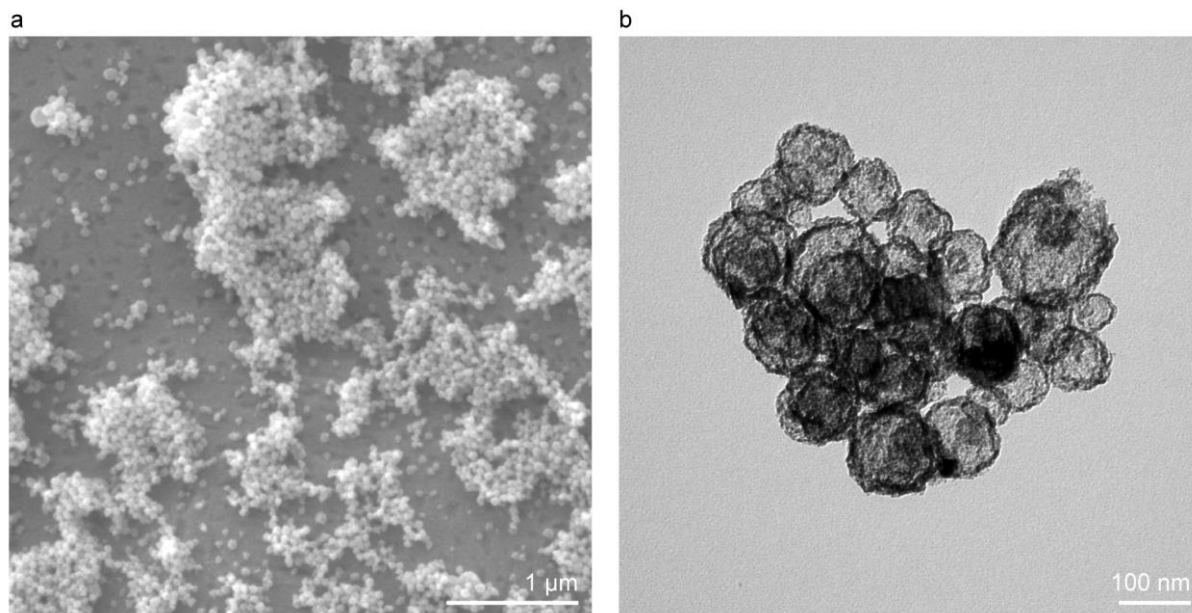


**Fig. S17.** (a) SEM and (b) TEM images of a yolk-shell composite prepared by immersing the PS<sub>480</sub>-*b*-P2VP<sub>490</sub> spherical micelle film on nickel foam in 1 mL of a diluted solution (0.1 mg/mL) of Ru<sup>3+</sup> ion in ethanol for 3 h, followed by pyrolysis at 300 °C for 4 h in air. The sample was peeled from the nickel foam by ultrasonication for the tests.

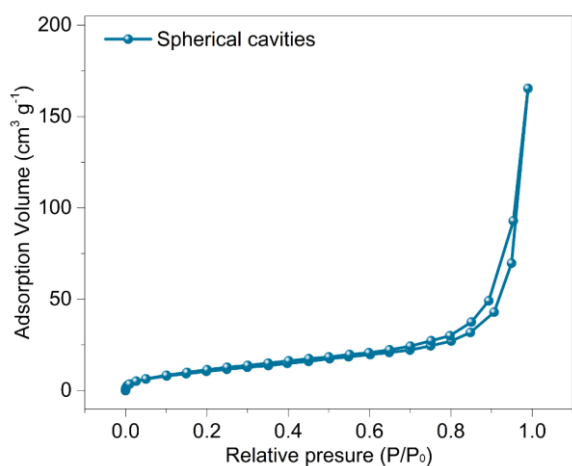


**Fig. S18.** Nitrogen sorption isotherm of Ru<sup>3+</sup>-derived mesoporous composite film with spherical cavities on nickel foam after pyrolysis at 300 °C in air. The sorption predominantly occurs in the  $P/P_0$  region of 0.8–0.9, indicative of the presence of relatively large mesopores (in consistent with the TEM results, pore diameter of 24.3 nm).

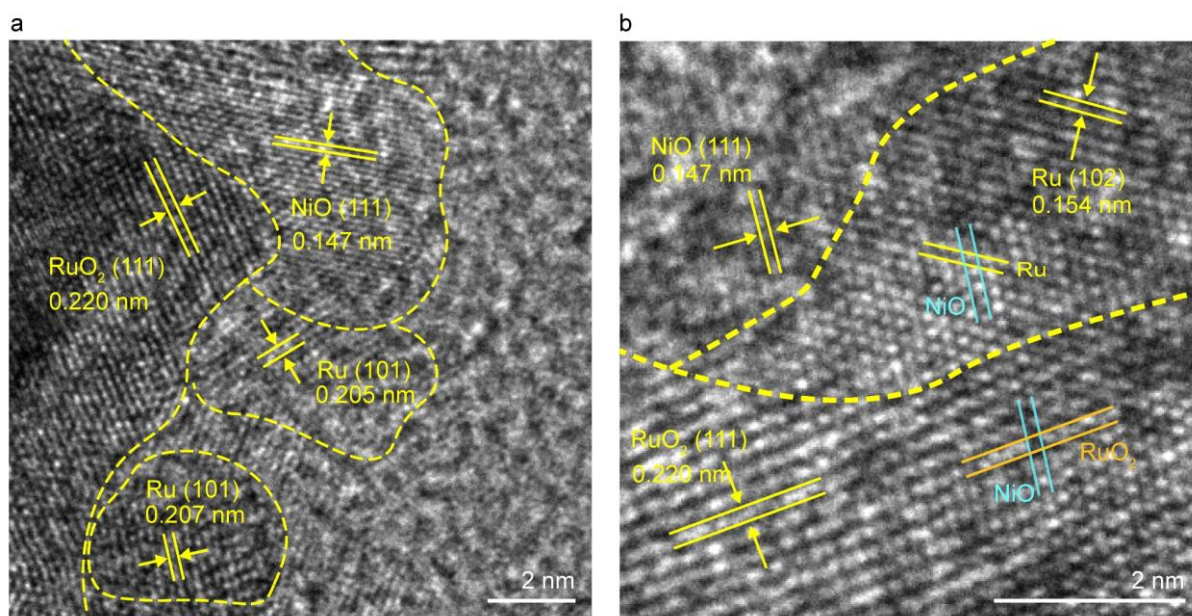


**Fig. S19.** HRTEM image of Ru<sup>3+</sup>-derived mesoporous composite film with spherical cavities on nickel foam formed after pyrolysis at 300 °C in air. The sample was peeled from the nickel foam by ultrasonication for the tests.

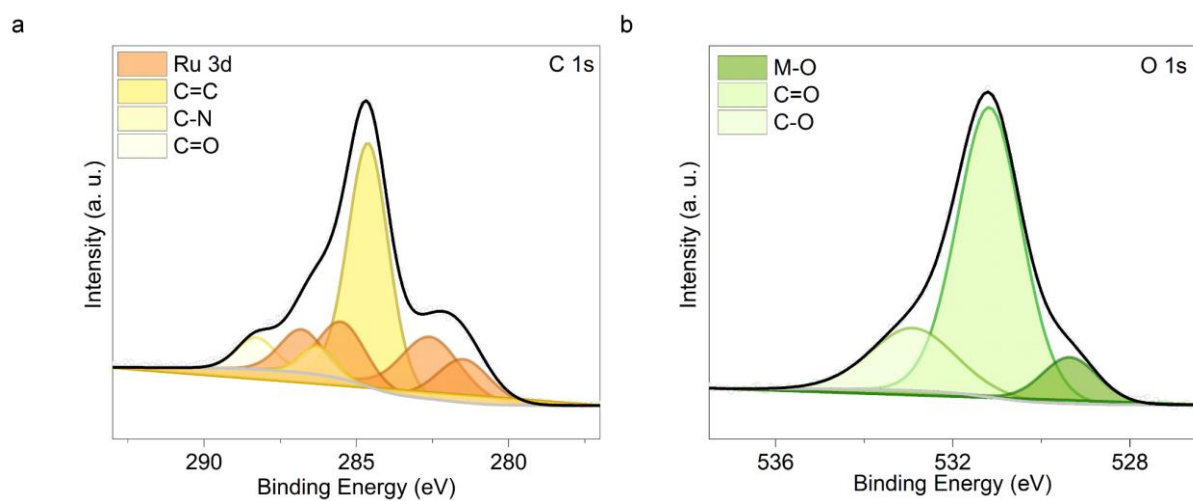


**Fig. S20.** High-resolution XPS spectra of (a) C 1s and (b) O 1s of Ru<sup>3+</sup>-derived mesoporous composite film with spherical cavities on nickel foam formed after pyrolysis at 300 °C in air.

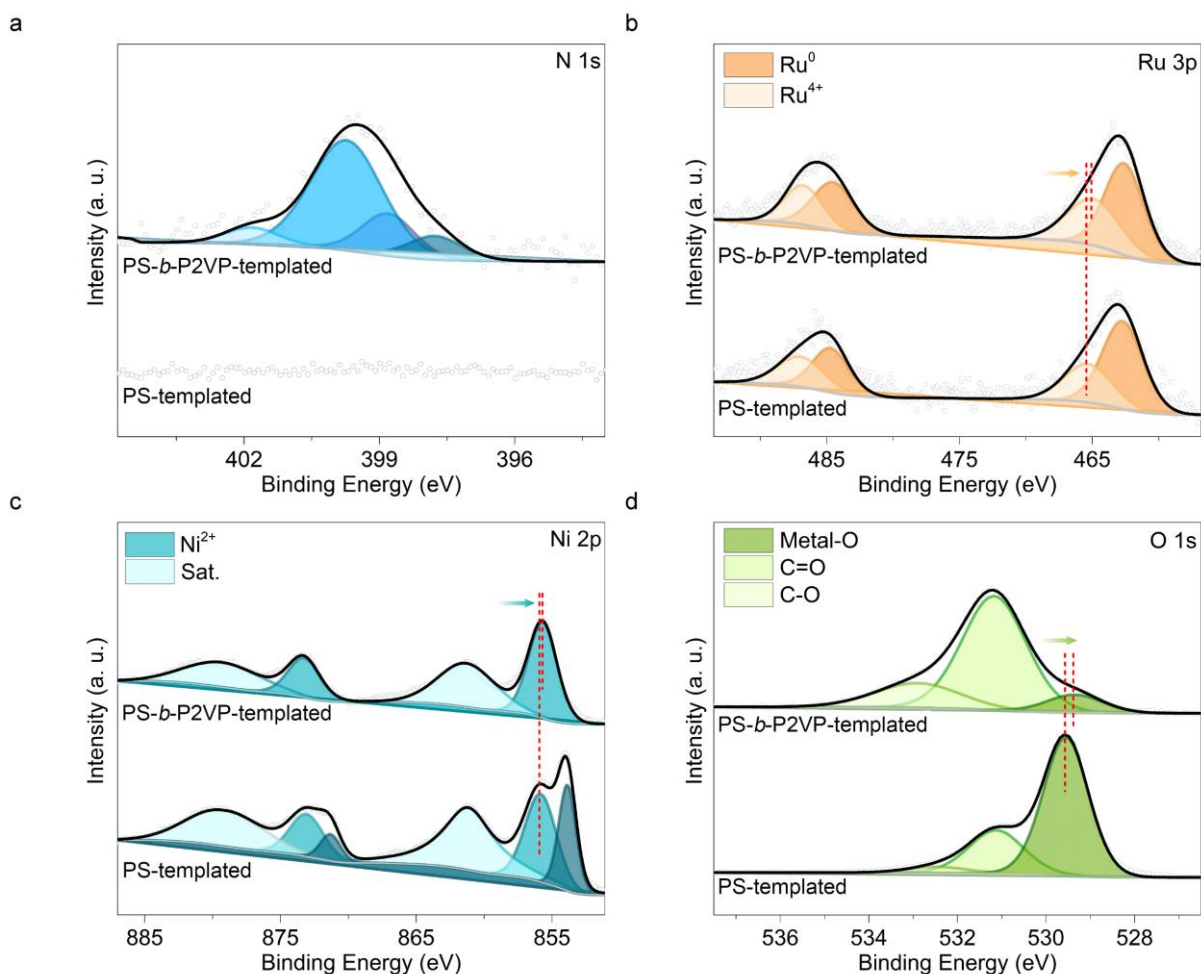


**Figure S21.** XPS spectra of (a) N 1s, (b) Ru 3p, and (c) Ni 2p, and (d) O 1s of PS microsphere-templated mesoporous composite film on nickel foam and PS-*b*-P2VP micelle film-templated mesoporous composite films on nickel foam. PS microsphere-templated mesoporous composite film on nickel foam was prepared by casting a solution of PS microspheres (the diameter of ca. 50 nm) in ethanol on nickel foam and subsequently immersed in Ru<sup>3+</sup> ions solution in an ethanol for 3 h, followed by the direct calcination at 300 °C in air. Compared to such N-free Ru/RuO<sub>2</sub>/NiO composites, the PS-*b*-P2VP micelle film-templated mesoporous composite films revealed negatively shifted characteristic peaks for both Ru<sup>4+</sup> (0.2 eV) and Ni<sup>2+</sup> (0.2 eV). It demonstrates the presence of N-doping, which renders an increase in the electron densities of Ru and Ni.<sup>8</sup> Moreover, the negative shift (0.3 eV) of metal–O component in O 1s spectra can be attributed to a decreased work function of PS-*b*-P2VP micelle film-templated mesoporous composite film, further verifying the successful N-doping.<sup>9</sup>

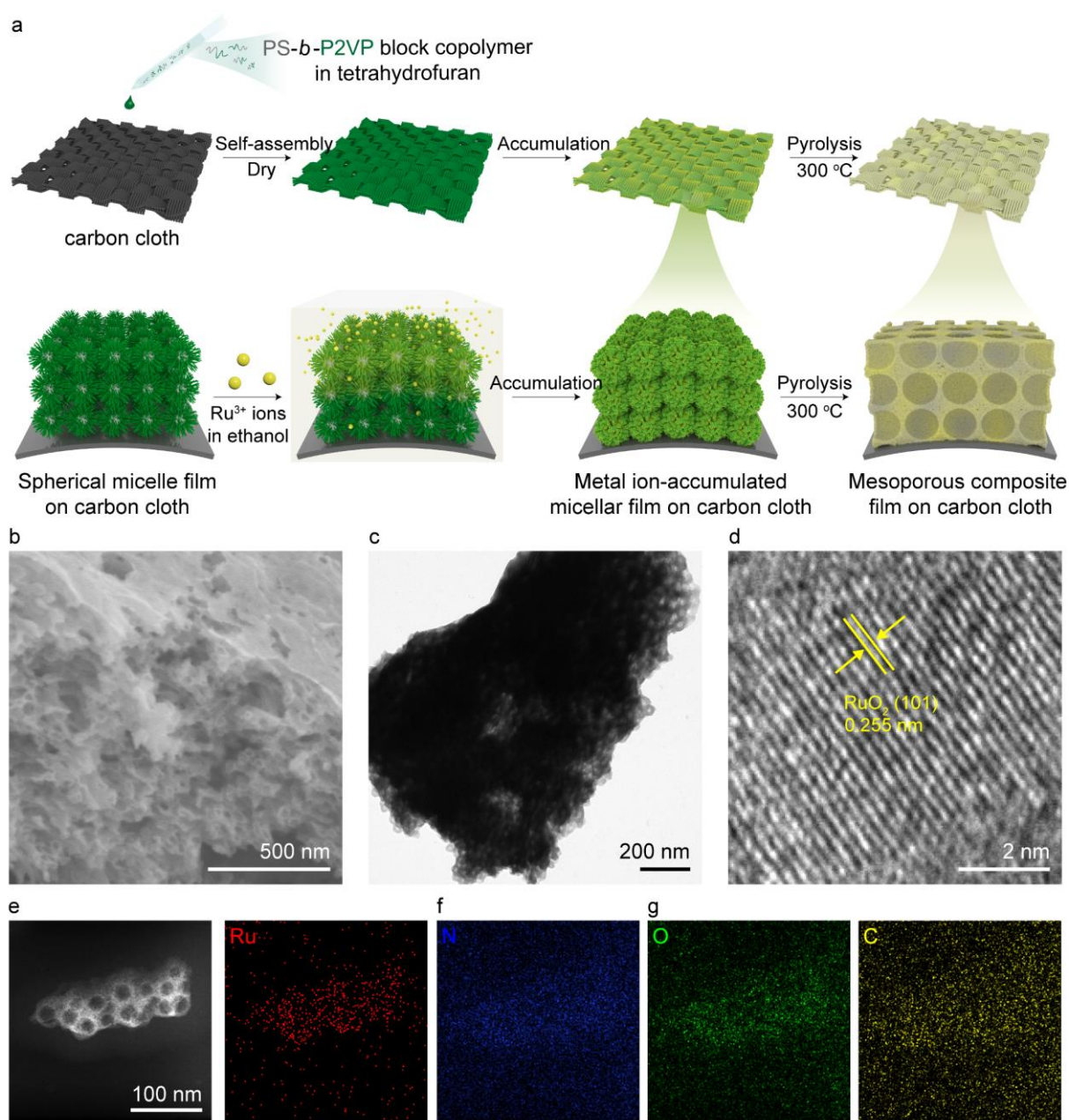


**Fig. S22.** (a) Schematic illustration of the formation of micellar film on carbon cloth and the subsequent accumulation of  $\text{Ru}^{3+}$  ions in an ethanol solution, followed by the direct conversion into mesoporous composite film upon pyrolysis at 300 °C. (b) SEM image, (c) TEM, (d) HRTEM and (e) elemental mapping images of mesoporous composite film on carbon cloth formed after pyrolysis. The sample was peeled from the carbon cloth by ultrasonication for the tests.

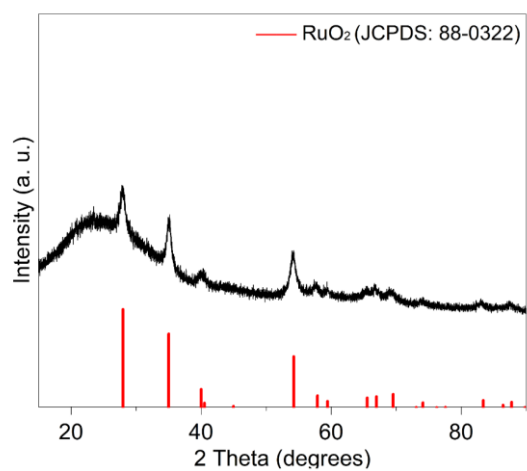


**Fig. S23.** XRD pattern of nitrogen doped RuO<sub>2</sub> (N-RuO<sub>2</sub>) mesoporous composite film with spherical cavities on carbon cloth.

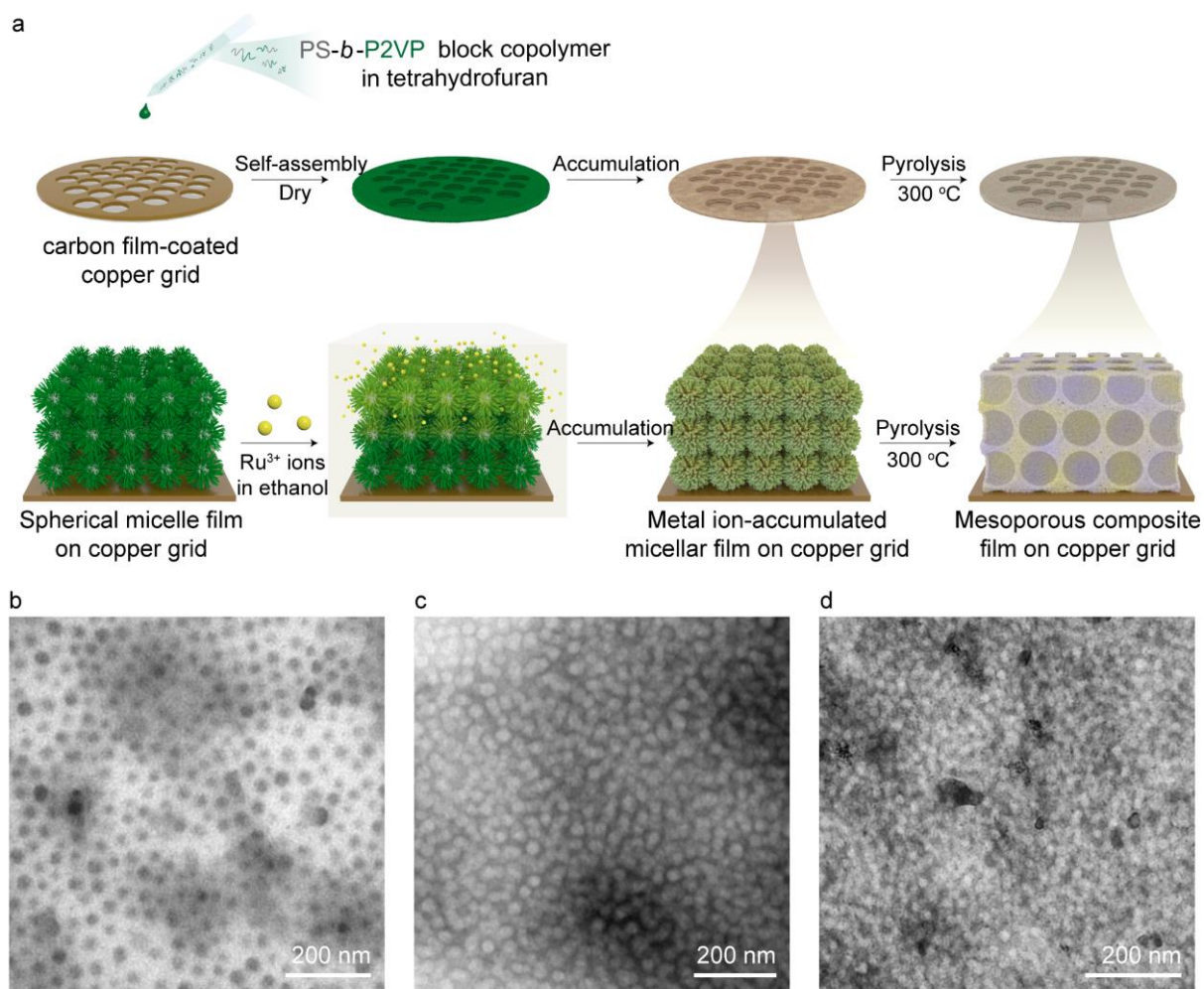


**Fig. S24.** (a) Schematic illustration of the formation of micellar film on carbon film-coated copper grid and the subsequent accumulation of Ru<sup>3+</sup> ions in an ethanol solution by dynamic coordination, followed by the direct conversion into mesoporous composite film upon pyrolysis at 300 °C. TEM images of (b) PS<sub>480</sub>-*b*-P2VP<sub>490</sub> micellar film on carbon film-coated copper grid, (c) metal ion-accumulated PS<sub>480</sub>-*b*-P2VP<sub>490</sub> micellar film on carbon film-coated copper grid, and (d) mesoporous composite film on carbon film-coated copper grid formed after pyrolysis at 300 °C in air.

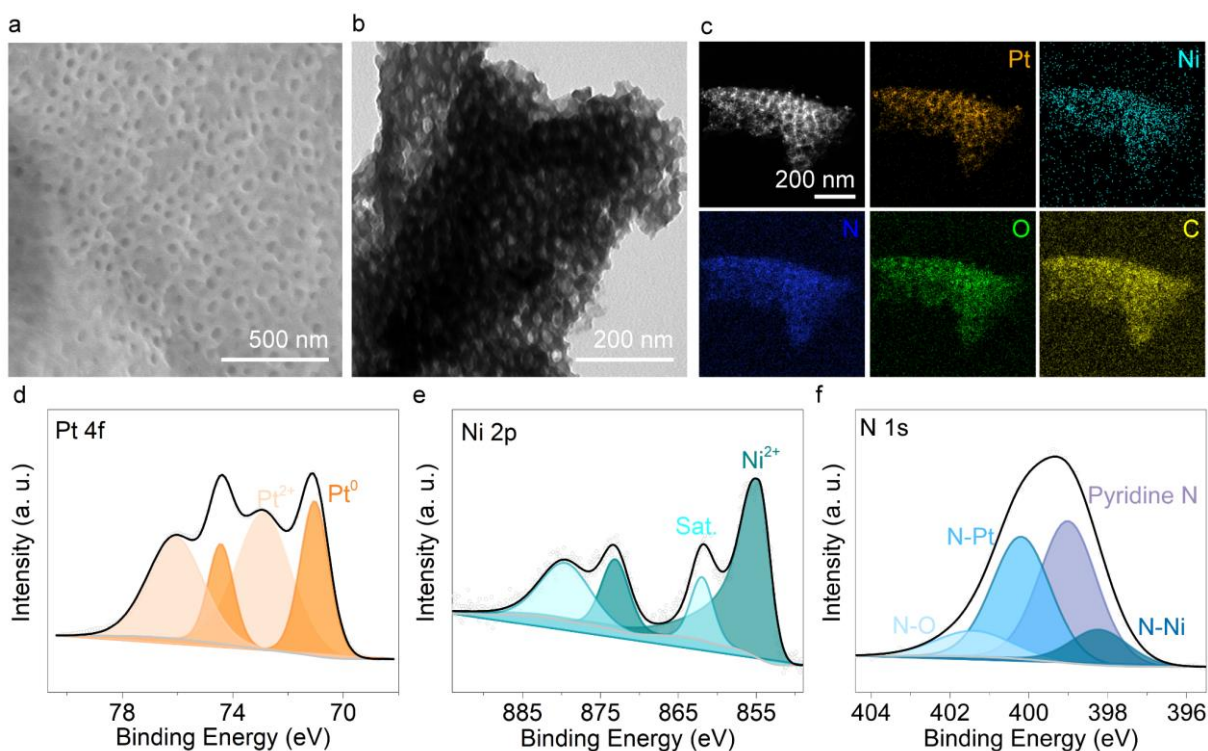


**Fig. S25.** (a) SEM image. (b) TEM, (c) elemental mapping images, and (d-f) high-resolution XPS spectra of (d) Pt 4f, (e) Ni 2p, and (f) N 1s of Pt<sup>2+</sup>-derived mesoporous composite films on nickel foam. Pt<sup>2+</sup>-derived mesoporous composite films on nickel foam were prepared by immersing the PS<sub>480</sub>-*b*-P2VP<sub>490</sub> micellar film on nickel foam in a solution of Pt<sup>2+</sup> ions in ethanol for 3 h, followed by the direct conversion upon pyrolysis at 300 °C in air for 4 h.

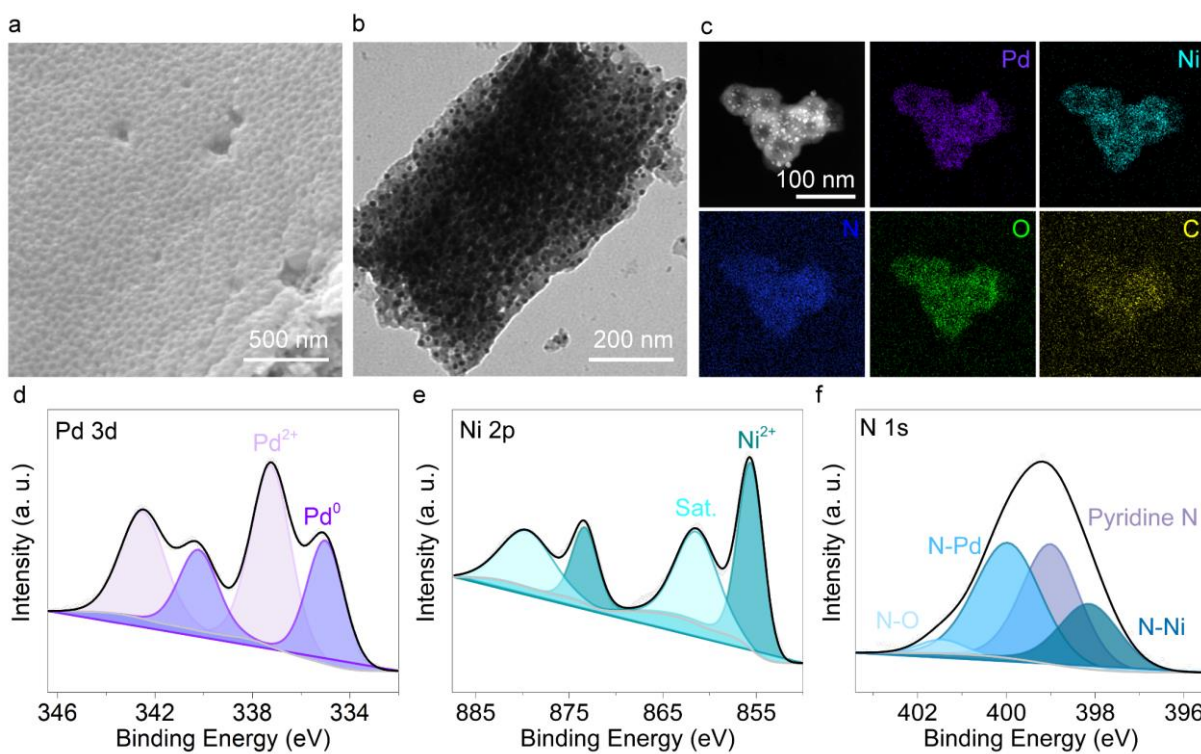


**Fig. S26.** (a) SEM image. (b) TEM, (c) elemental mapping images, and (d-f) high-resolution XPS spectra of (d) Pd 3d, (e) Ni 2p, and (f) N 1s of Pd<sup>2+</sup>-derived mesoporous composite films on nickel foam. Pd<sup>2+</sup>-derived mesoporous composite films on nickel foam were prepared by immersing the PS<sub>480</sub>-*b*-P2VP<sub>490</sub> micellar film on nickel foam in a solution of Pd<sup>2+</sup> ions in ethanol for 3 h, followed by the direct conversion upon pyrolysis at 300 °C in air.

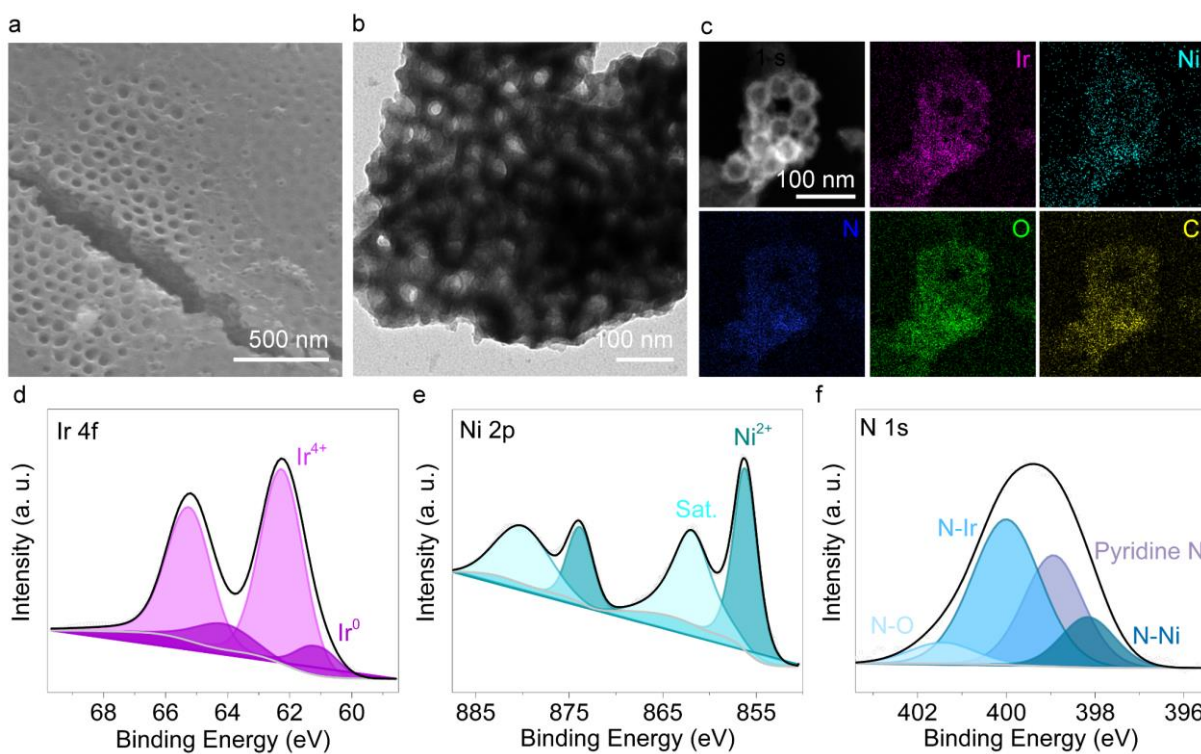


**Fig. S27.** (a) SEM image. (b) TEM, (c) elemental mapping images, and (d-f) high-resolution XPS spectra of (d) Ir 4f, (e) Ni 2p, and (f) N 1s of Ir<sup>3+</sup>-derived mesoporous composite films on nickel foam. Ir<sup>3+</sup>-derived mesoporous composite films on nickel foam were prepared by immersing the PS<sub>480</sub>-*b*-P2VP<sub>490</sub> micellar film on nickel foam in a solution of Ir<sup>3+</sup> ions in ethanol for 3 h, followed by the direct conversion upon pyrolysis at 300 °C in air.

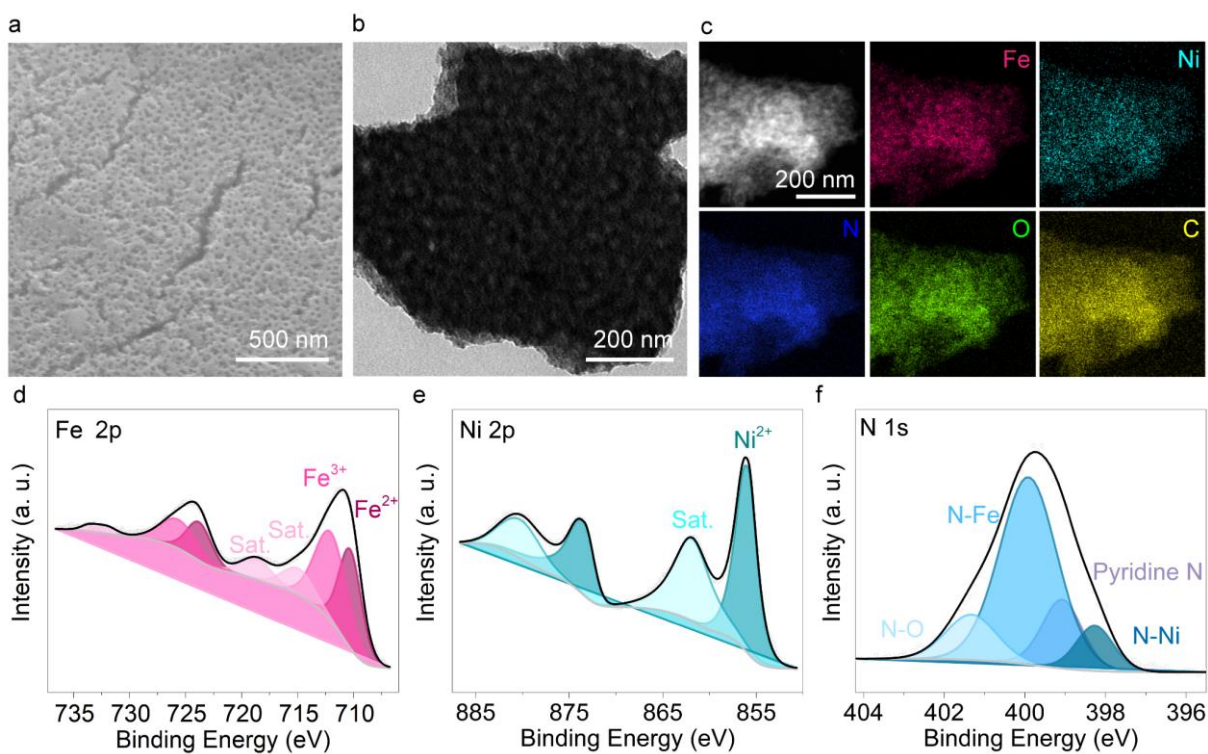


**Fig. S28.** (a) SEM image. (b) TEM, (c) elemental mapping images, and (d-f) high-resolution XPS spectra of (d) Fe 3p, (e) Ni 2p, and (f) N 1s of Fe<sup>3+</sup>-derived mesoporous composite films on nickel foam. Fe<sup>3+</sup>-derived mesoporous composite films on nickel foam were prepared by immersing the PS<sub>480</sub>-*b*-P2VP<sub>490</sub> micellar film on nickel foam in a solution of Fe<sup>3+</sup> ions in ethanol for 3 h, followed by the direct conversion upon pyrolysis at 300 °C in air.

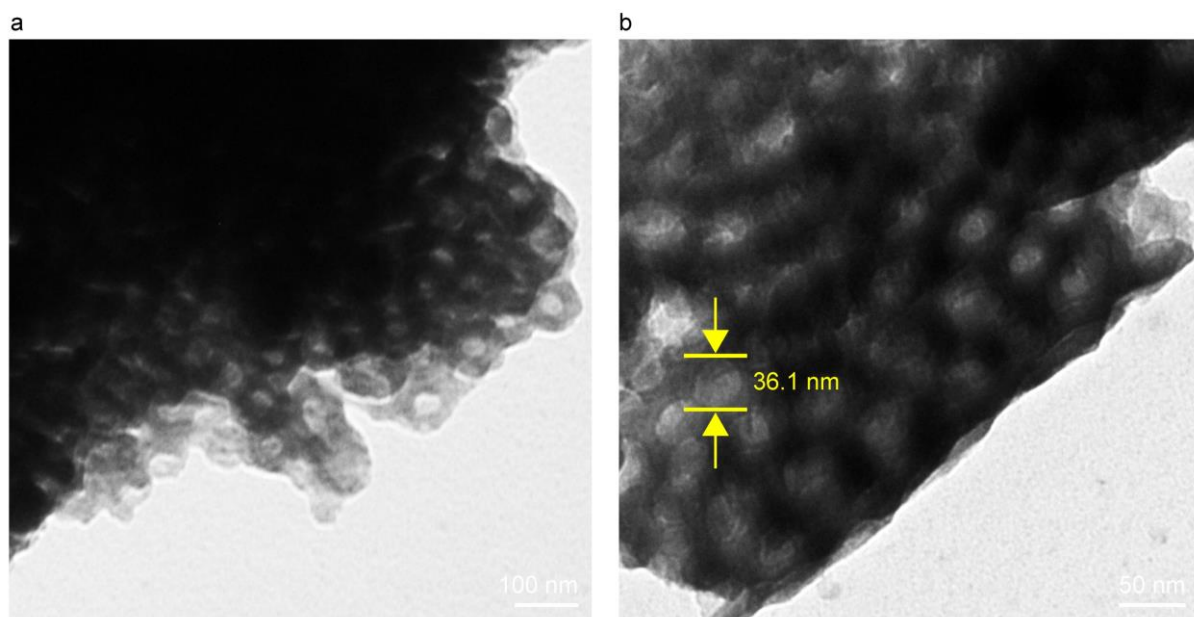


**Fig. S29.** TEM image of mesoporous composite film prepared by immersing the PS<sub>870</sub>-*b*-P2VP<sub>1430</sub> micellar film on silicon wafer in solution of Ru<sup>3+</sup> ion in ethanol for 3 h, followed by pyrolysis at 300 °C for 4 h in air.

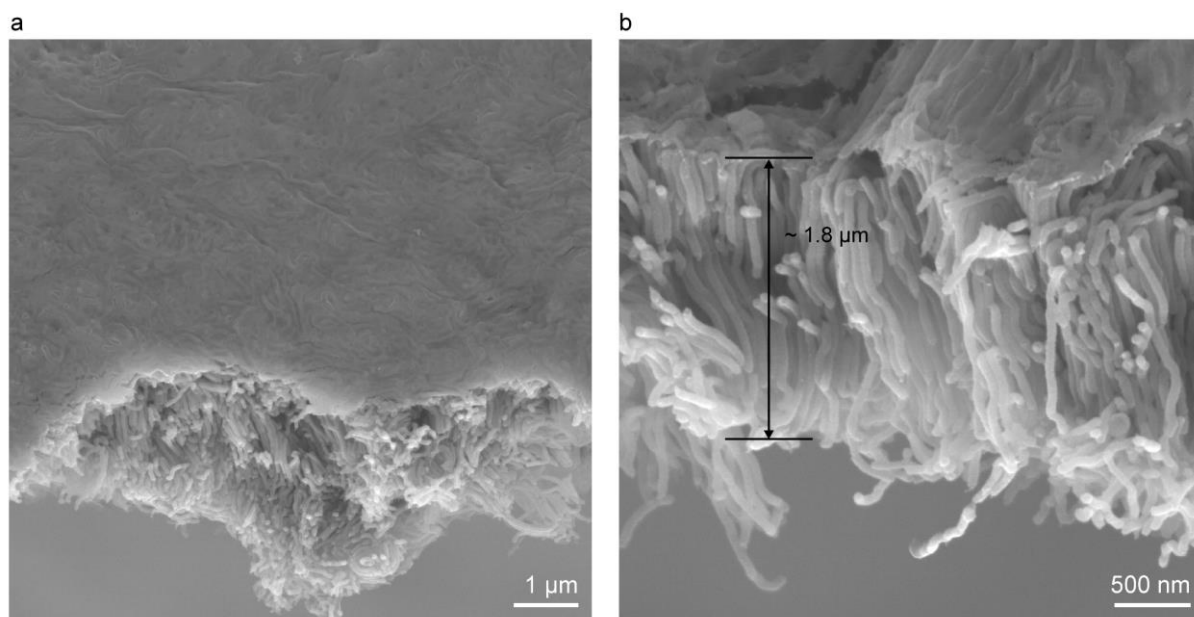


**Fig. S30.** SEM images of Ru<sup>3+</sup>-derived cylindrical micelle film on nickel foam.

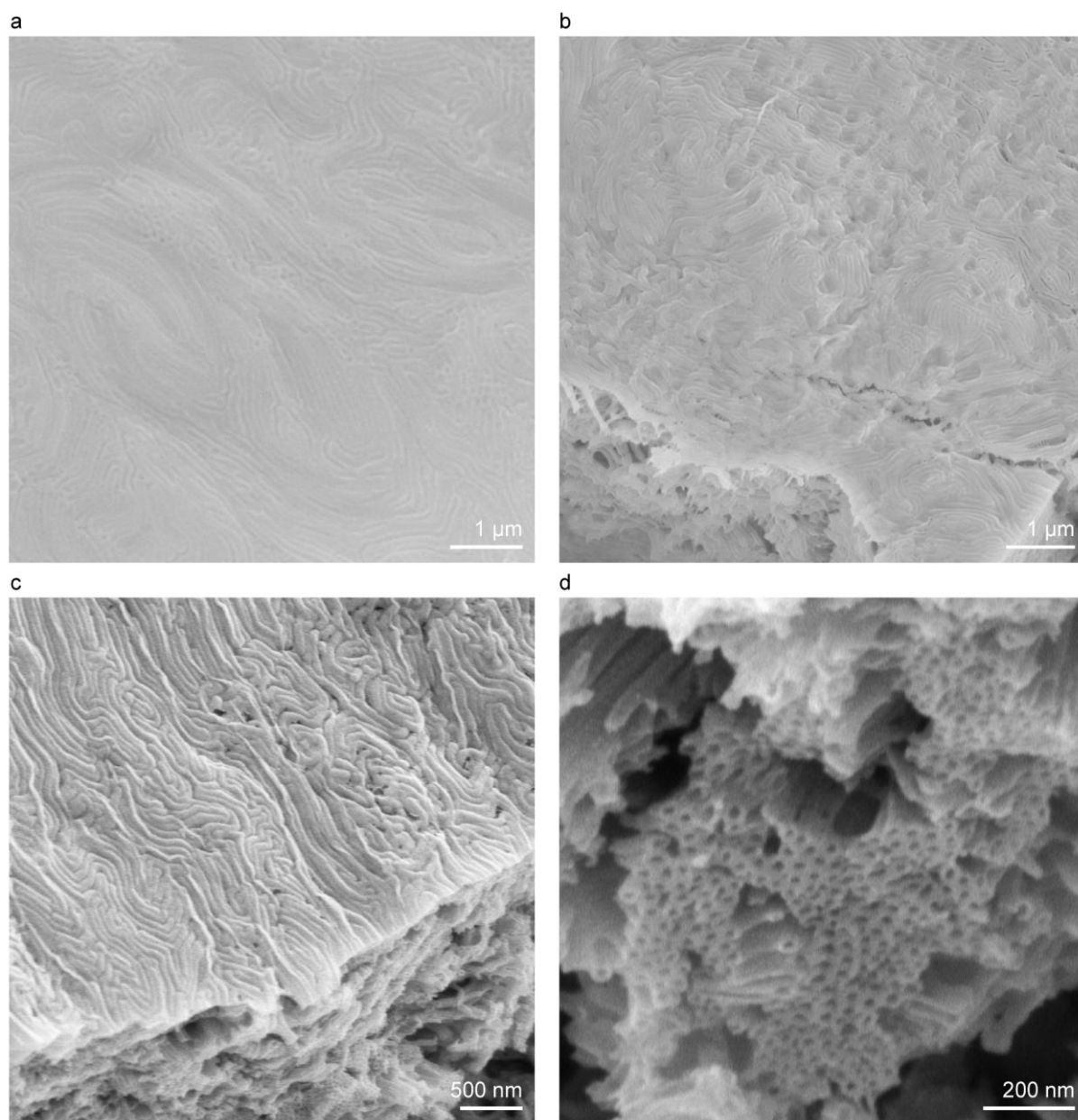


**Fig. S31.** SEM images of the (a) surface of central region, (b) surface of edge region, (c) fracture surface and (d) fracture edge of Ru<sup>3+</sup>-derived mesoporous composite film with cylindrical cavities on nickel foam formed after pyrolysis at 300 °C in air.

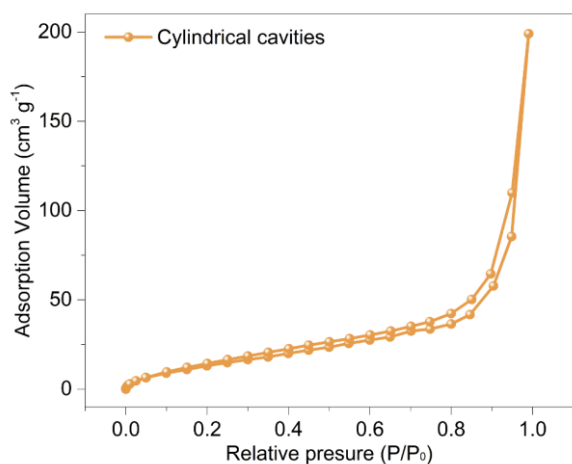


**Fig. S32.** Nitrogen sorption isotherm of Ru<sup>3+</sup>-derived mesoporous composite films with cylindrical cavities on nickel foam after pyrolysis at 300 °C in air. The sorption predominantly occurs in the  $P/P_0$  region of 0.8–0.9, indicative of the presence of relatively large mesopores (in consistent with the TEM results, pore diameter of 17.2 nm).

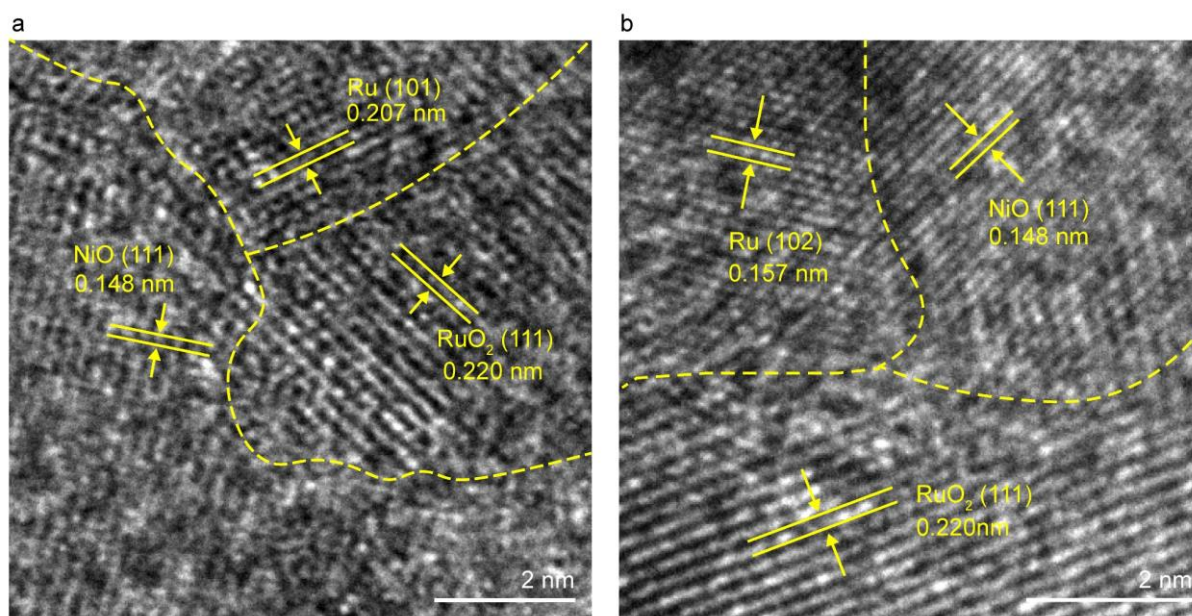


**Fig. S33.** HRTEM image of Ru<sup>3+</sup>-derived mesoporous composite film with cylindrical cavities on nickel foam formed after pyrolysis at 300 °C in air.

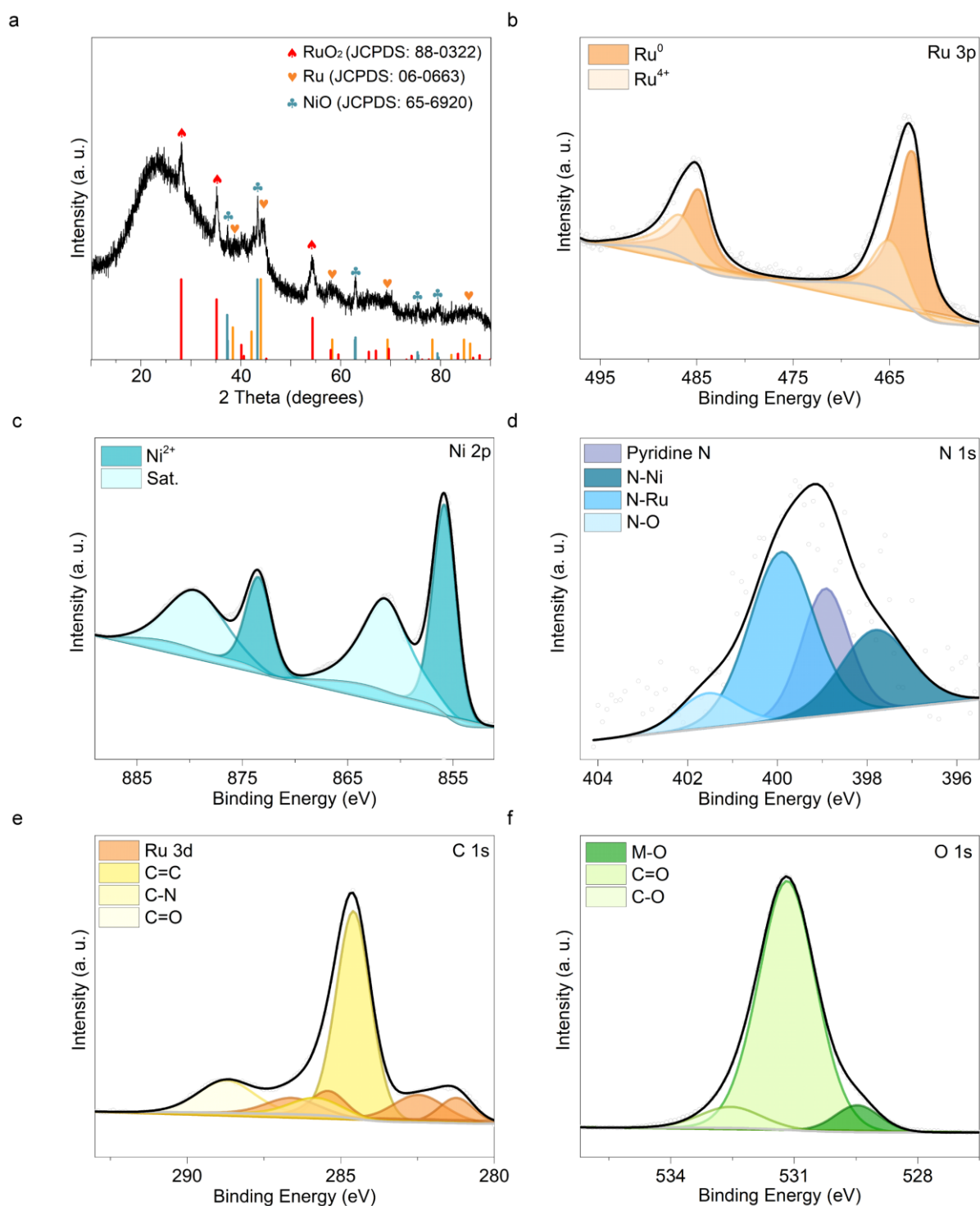


**Fig. S34.** (a) XRD pattern of  $\text{Ru}^{3+}$ -derived mesoporous composite film with cylindrical cavities that peeled from nickel foam by ultrasonication. (b-f) High-resolution XPS spectra of (b) Ru 3p, (c) Ni 2p, (d) N 1s, (e) C 1s, and (f) O 1s of  $\text{Ru}^{3+}$ -derived mesoporous composite film with cylindrical cavities on nickel foam.

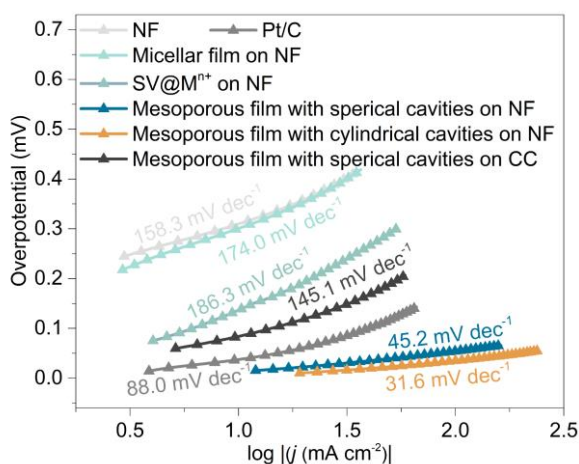


**Fig. S35.** Tafel slopes for HER of Pt/C, nickel foam, micellar film on nickel foam (NF), metal ion-accumulated micellar film on nickel foam, mesoporous N-Ru/RuO<sub>2</sub>/NiO composite film with spherical cavities on nickel foam, mesoporous N-Ru/RuO<sub>2</sub>/NiO composite film with cylindrical cavities on nickel foam, and mesoporous N-RuO<sub>2</sub> composite film with spherical cavities on carbon cloth (CC).

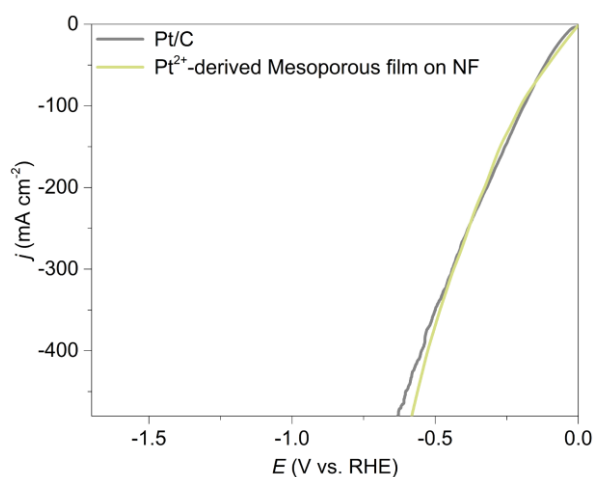


**Fig. S36.** HER linear sweep voltammetry (LSV) curves with *iR*-correction for Pt/C and Pt<sup>2+</sup>-derived Mesoporous film on nickel foam (NF). The Pt-derived mesoporous film with spherical cavities revealed lower overpotential (21 mV) than the commercial Pt/C (42 mV) at a current density of 10 mA cm<sup>-2</sup>. At a high current density of 200 mA cm<sup>-2</sup>, the Pt<sup>2+</sup>-derived mesoporous film showed a similar overpotential (322 mV) to commercial Pt/C (321 mV).

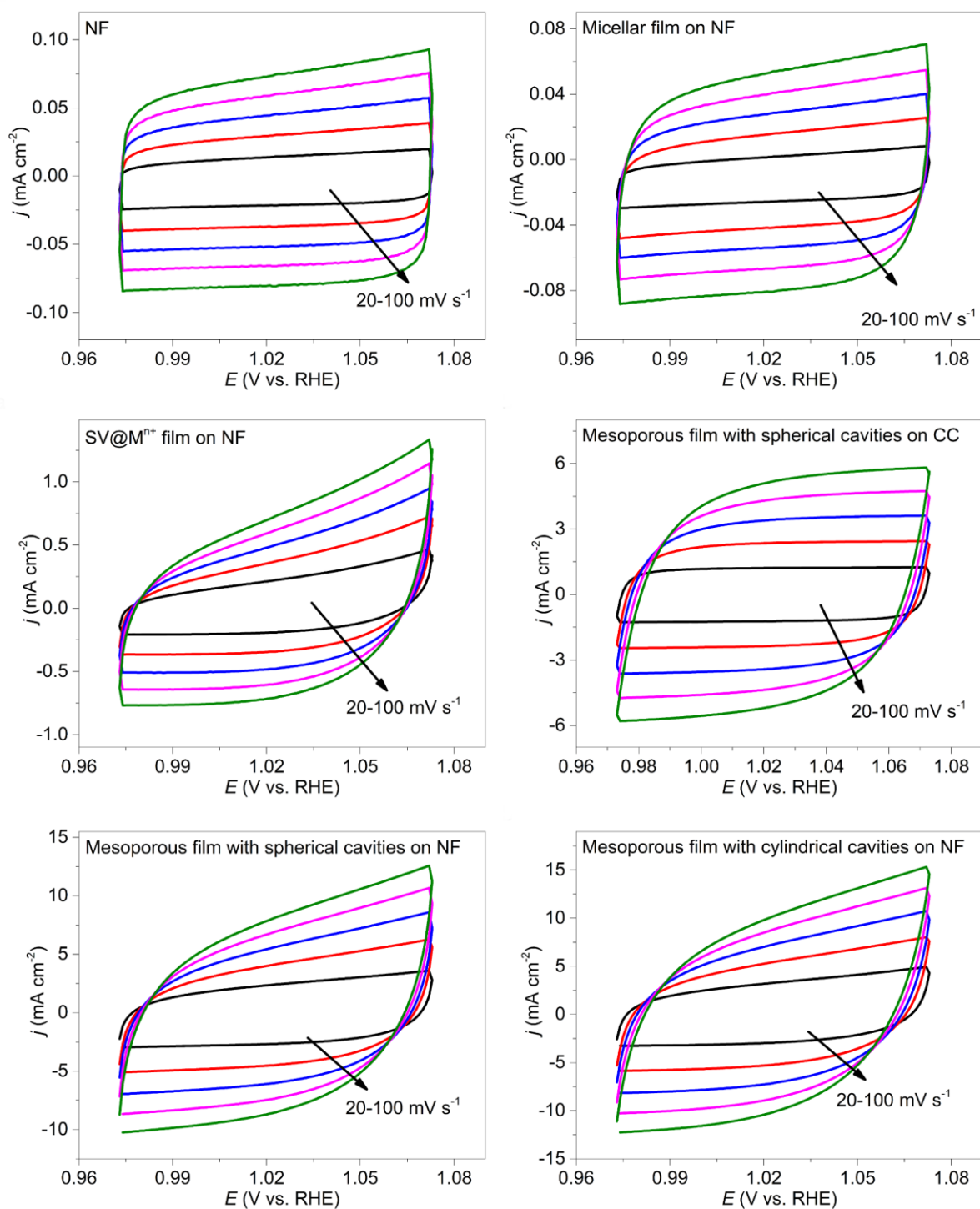


**Fig. S37.** CV curves of nickel foam, micellar film on nickel foam, metal ion-accumulated micellar film on nickel foam, mesoporous N-Ru/RuO<sub>2</sub>/NiO composite film with spherical cavities on nickel foam, mesoporous N-Ru/RuO<sub>2</sub>/NiO composite film with cylindrical cavities on nickel foam, and mesoporous N-RuO<sub>2</sub> composite film with spherical cavities on carbon cloth at increasing scan rates of 20–100 mV s<sup>-1</sup> in 1.0 M KOH.

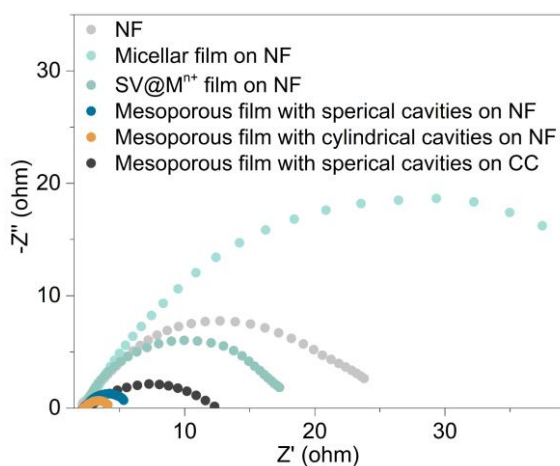


**Fig. S38.** EIS Nyquist plots for OER of nickel foam, micellar film on nickel foam, metal ion-accumulated micellar film on nickel foam, mesoporous N-Ru/RuO<sub>2</sub>/NiO composite film with spherical cavities on nickel foam, mesoporous N-Ru/RuO<sub>2</sub>/NiO composite film with cylindrical cavities on nickel foam, and mesoporous N-RuO<sub>2</sub> composite film with spherical cavities on carbon cloth (CC).

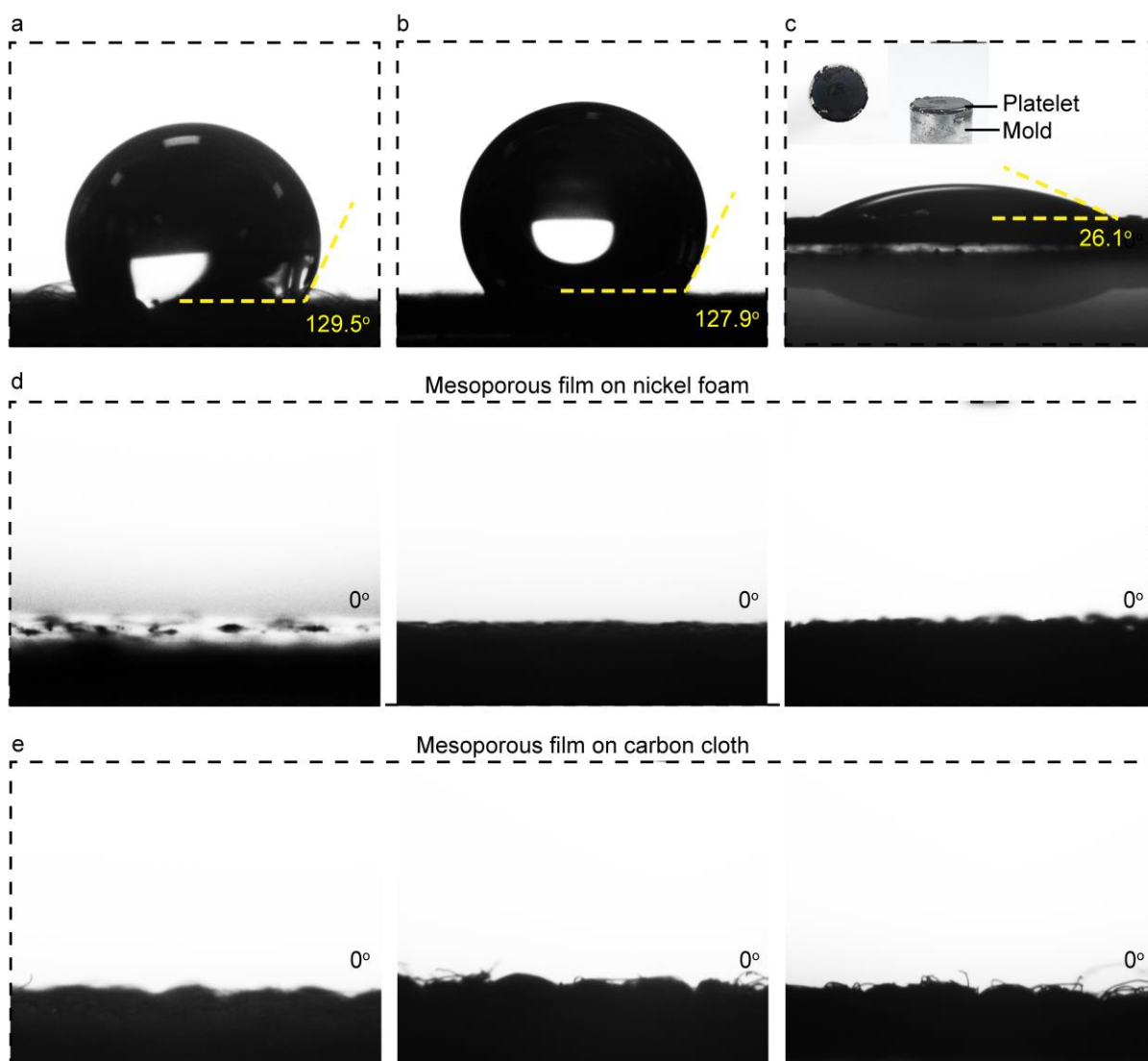


**Fig. S39.** Contact angles of (a) bare nickel foam, (b) bare carbon cloth, (c) a platelet of Ru/RuO<sub>2</sub>/NiO composite powder (the powder was placed in a steel mold with a load of 0.02 tons for 5 min to form a platelet), (d) mesoporous N-Ru/RuO<sub>2</sub>/NiO composite films on nickel foam, and (e) mesoporous N-RuO<sub>2</sub> composite films on carbon cloth.

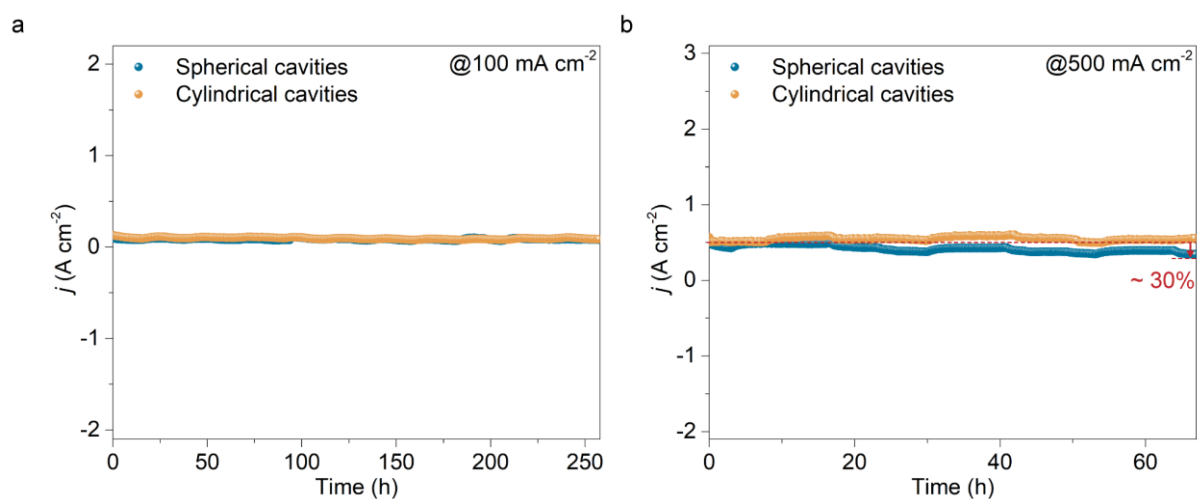


**Fig. S40.** Chronoamperometry curve of mesoporous N-Ru/RuO<sub>2</sub>/NiO composite films with spherical and cylindrical cavities on nickel foam toward overall water splitting at (a) 100 mA cm<sup>-2</sup> and (b) 500 mA cm<sup>-2</sup>.

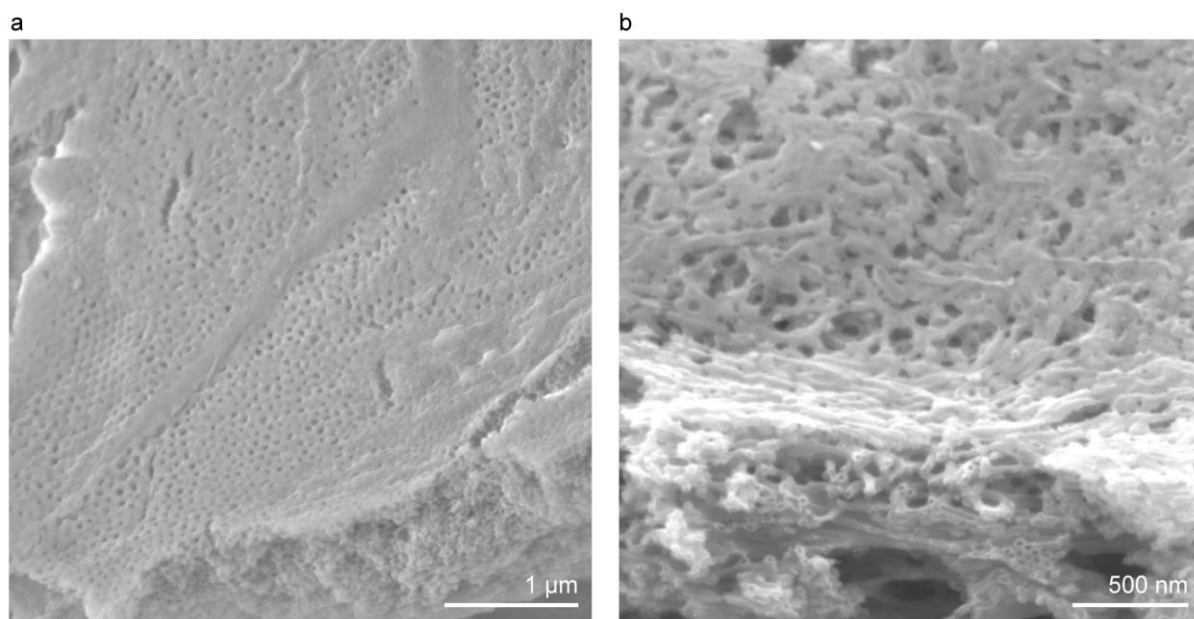


**Fig. S41.** SEM images of mesoporous N-Ru/RuO<sub>2</sub>/NiO composite films with (a) spherical and (b) cylindrical cavities on nickel foam after the stability test at 100 mA cm<sup>-2</sup>.

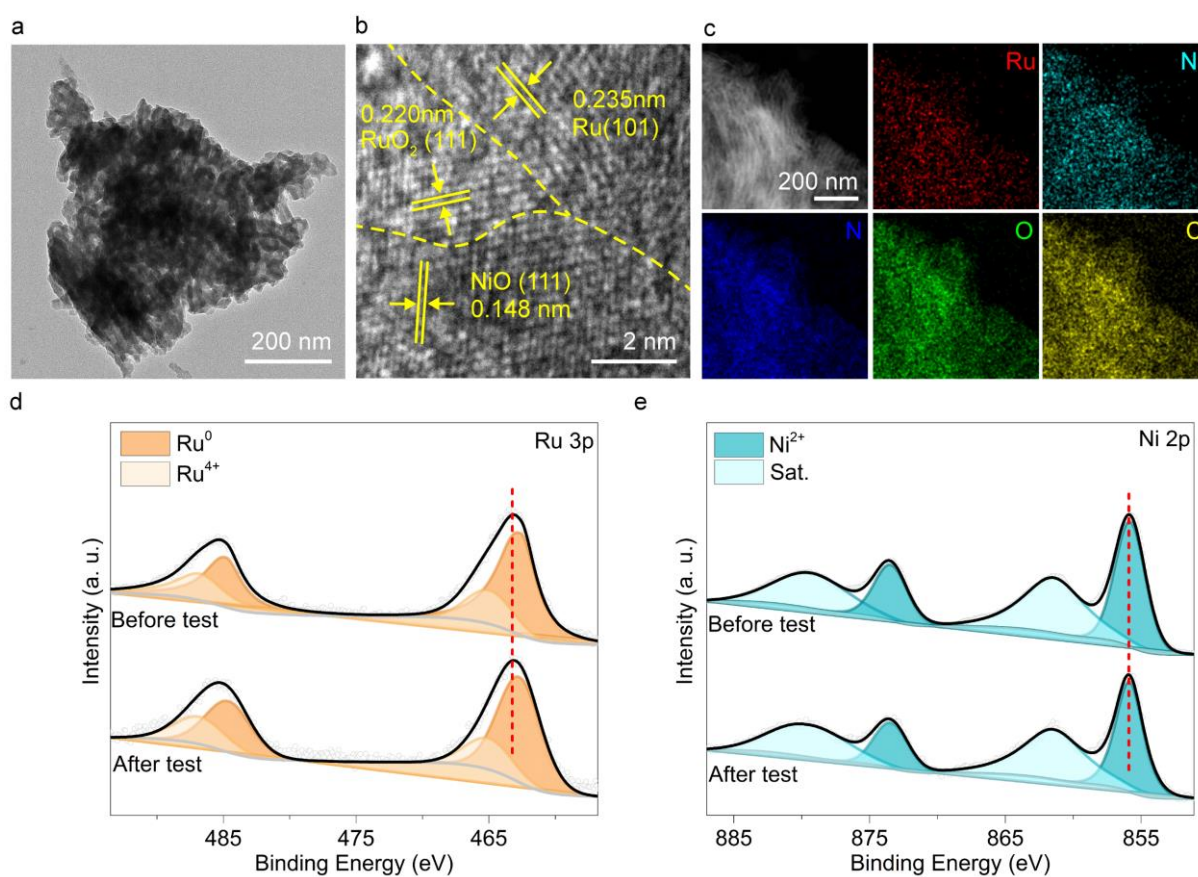


**Fig. S42.** (a) TEM, (b) HRTEM, and (c) elemental mapping images of mesoporous N-Ru/RuO<sub>2</sub>/NiO composite films with cylindrical cavities on nickel foam after the HER stability test. (d, e) High-resolution XPS spectra of (d) Ru 3p and (e) Ni 2p of mesoporous N-Ru/RuO<sub>2</sub>/NiO composite films with cylindrical cavities on nickel foam before and after the HER stability test.

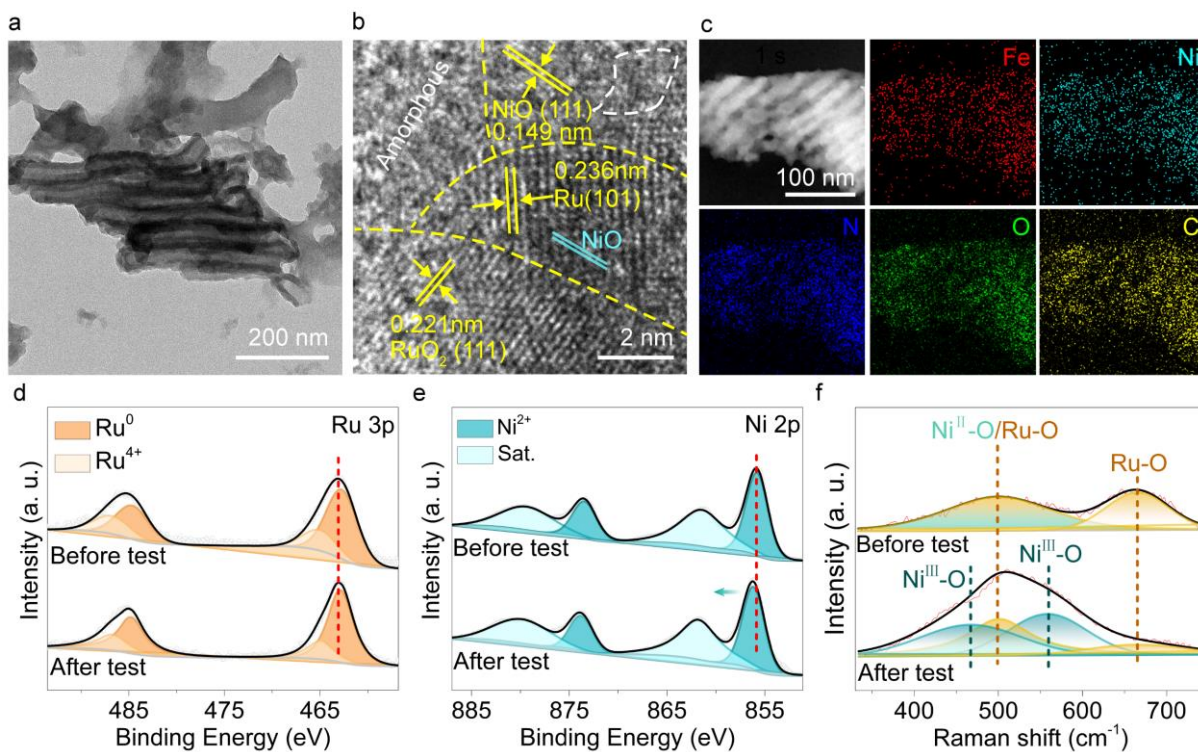


**Fig. S43.** (a) TEM, (b) HRTEM, and (c) elemental mapping images of mesoporous N-Ru/RuO<sub>2</sub>/NiO composite films with cylindrical cavities on nickel foam after the OER stability test. (d, e) High-resolution XPS spectra of (d) Ru 3p and (e) Ni 2p, and (f) Raman spectra of mesoporous N-Ru/RuO<sub>2</sub>/NiO composite films with cylindrical cavities on nickel foam before and after the OER stability test.

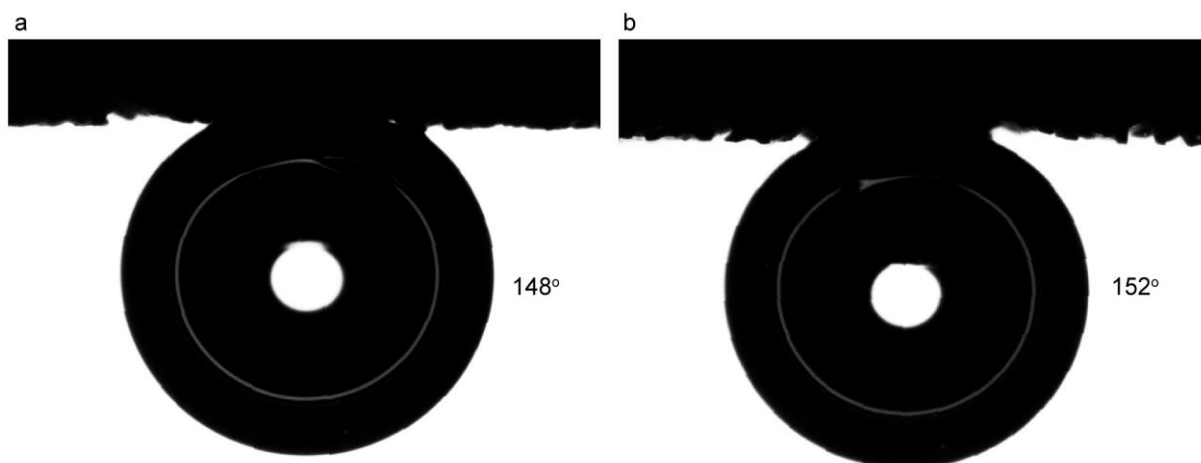


**Fig. S44.** Air contact angles of mesoporous N-Ru/RuO<sub>2</sub>/NiO composite films with (a) spherical and (b) cylindrical cavities on nickel foam.

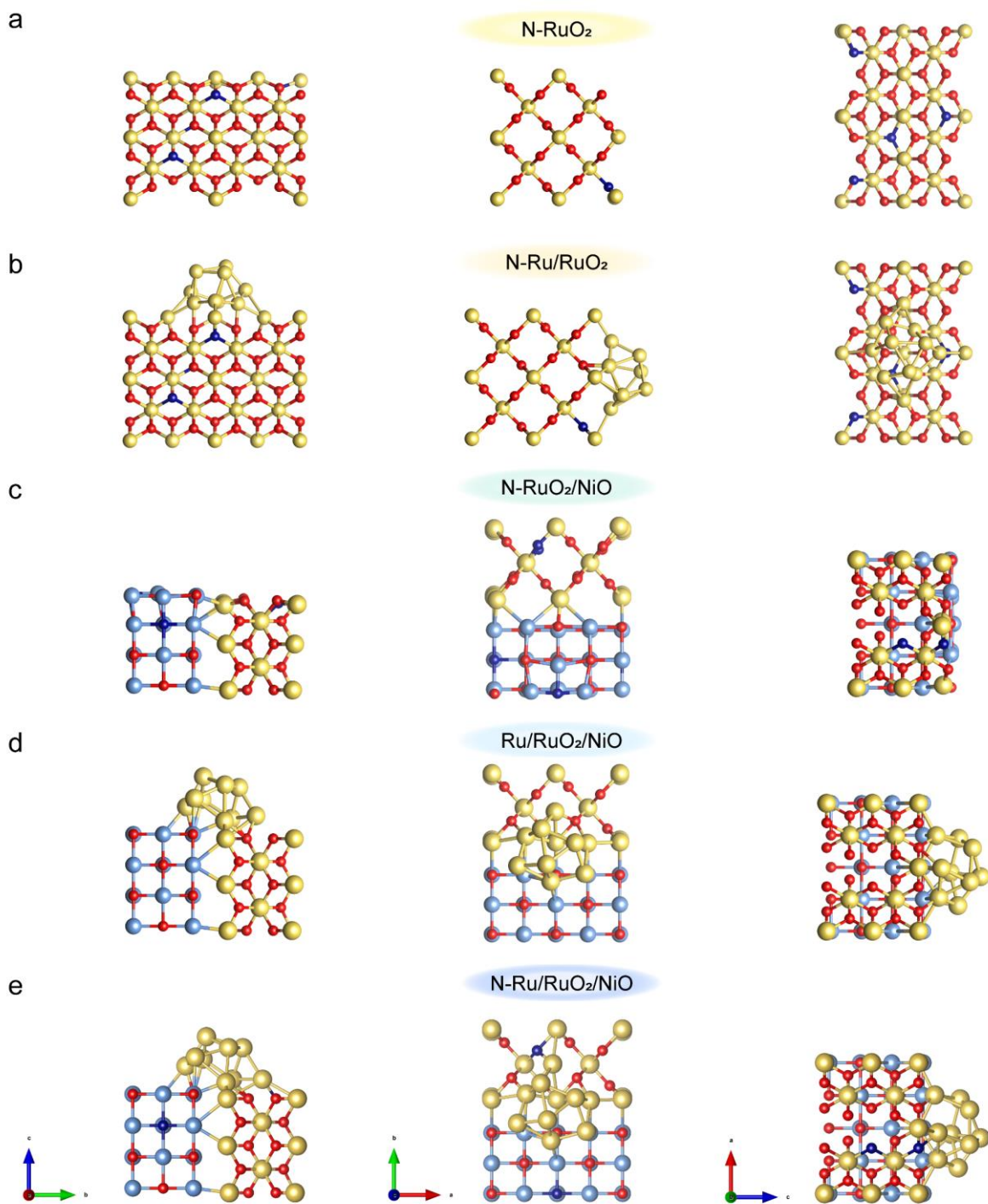


**Fig. S45.** Optimized atomic configurations of (a) nitrogen-doped  $\text{RuO}_2$  (N- $\text{RuO}_2$ ), (b) nitrogen-doped  $\text{Ru}/\text{RuO}_2$  (N- $\text{Ru}/\text{RuO}_2$ ), (c) nitrogen-doped  $\text{RuO}_2/\text{NiO}$  (N- $\text{RuO}_2/\text{NiO}$ ), (d)  $\text{Ru}/\text{RuO}_2/\text{NiO}$ , and (e) nitrogen-doped  $\text{Ru}/\text{RuO}_2/\text{NiO}$  (N- $\text{Ru}/\text{RuO}_2/\text{NiO}$ ) composite models under different viewpoints. The yellow, blue, dark blue and red balls represent Ru, Ni, N, and O atoms, respectively.

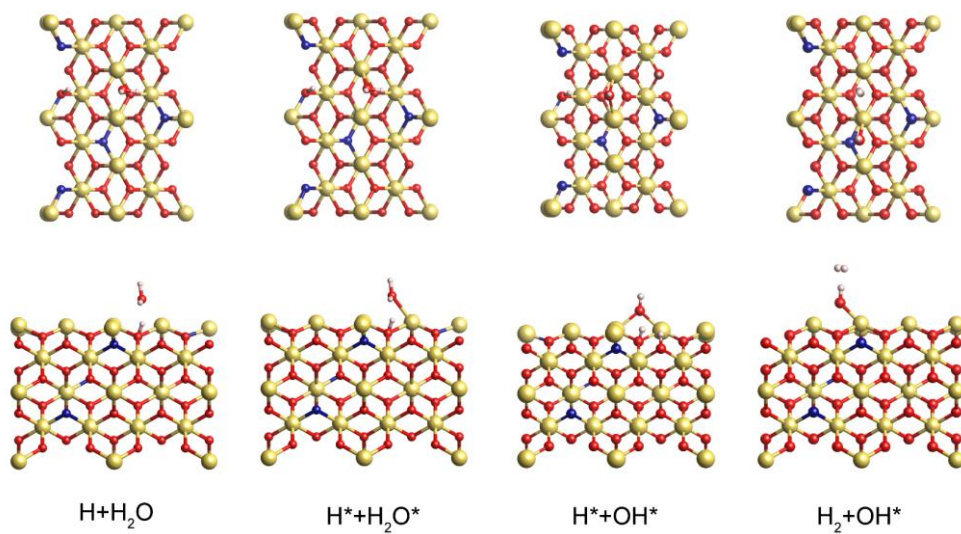


**Fig. S46.** Corresponding atomic structures of N-RuO<sub>2</sub> for the reaction pathway in HER. The yellow, dark blue, red and pink balls represent Ru, N, O and H atoms, respectively.

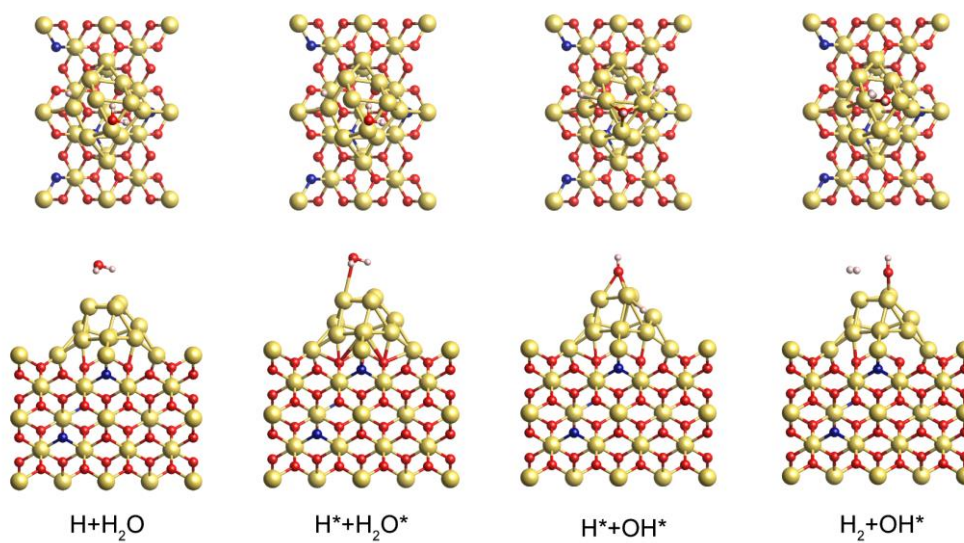


**Fig. S47.** Corresponding atomic structures of N-Ru/RuO<sub>2</sub> for the reaction pathway in HER. The yellow, dark blue, red and pink balls represent Ru, N, O and H atoms, respectively.

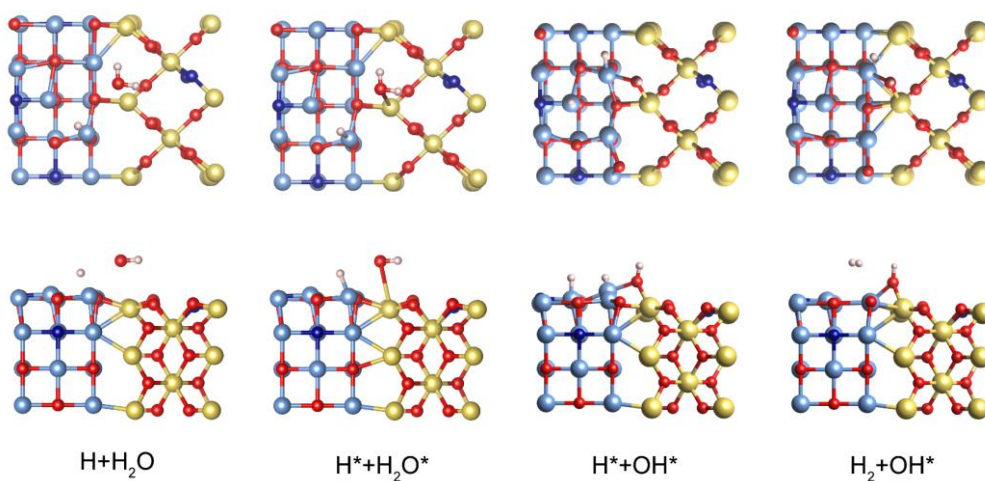


**Fig. S48.** Corresponding atomic structures of N-RuO<sub>2</sub>/NiO for the reaction pathway in HER. The yellow, blue, dark blue, red and pink balls represent Ru, Ni, N, O and H atoms, respectively.

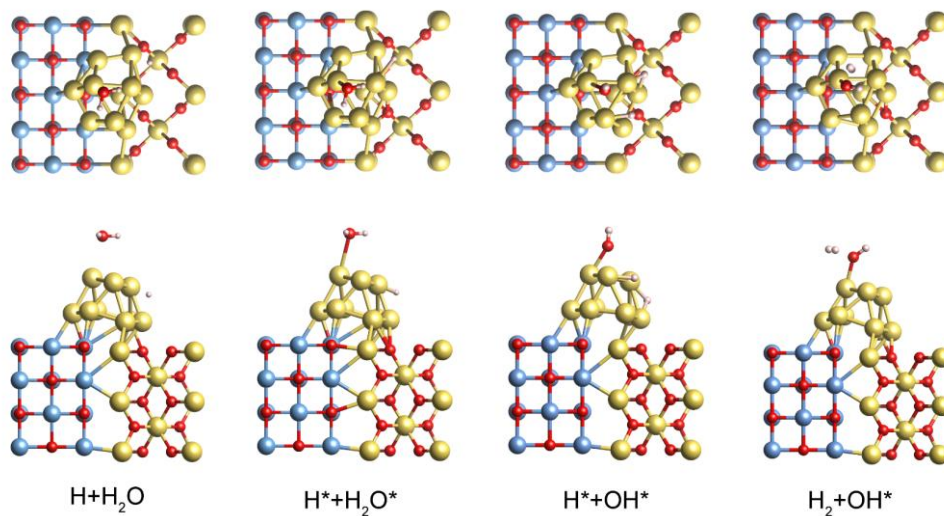


**Fig. S49.** Corresponding atomic structures of Ru/RuO<sub>2</sub>/NiO for the reaction pathway in HER. The yellow, blue, red and pink balls represent Ru, Ni, O and H atoms, respectively.

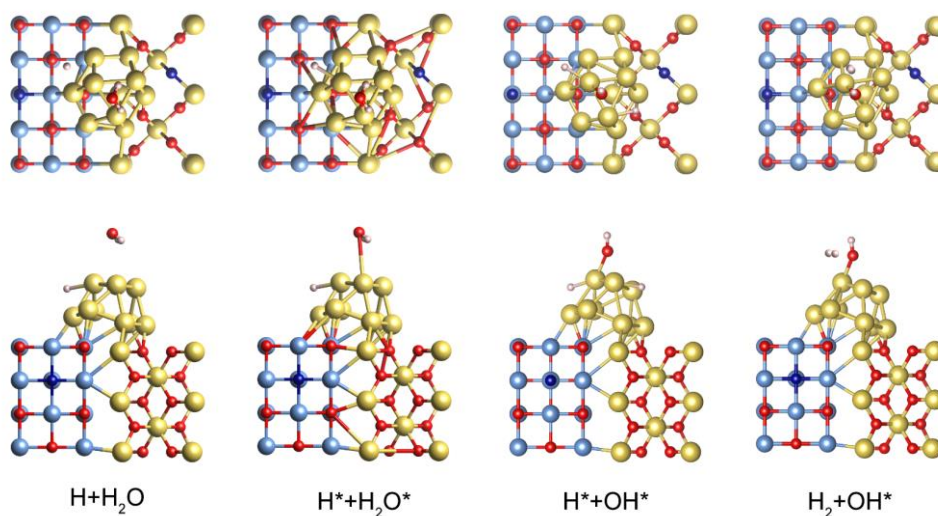


**Fig. S50.** Corresponding atomic structures of N-Ru/RuO<sub>2</sub>/NiO for the reaction pathway in HER. The yellow, blue, dark blue, red and pink balls represent Ru, Ni, N, O and H atoms, respectively.

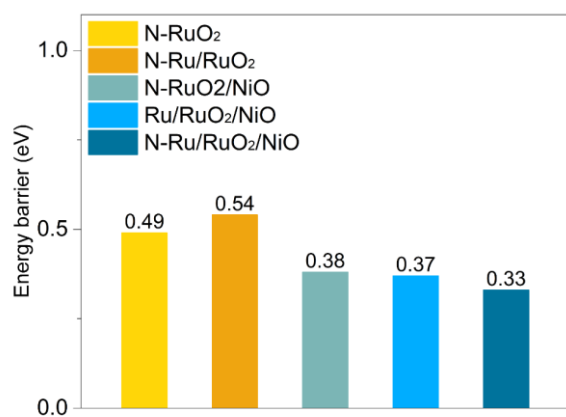


**Fig. S51.** Dissociation energy barrier of the rate-determining step in HER for N-RuO<sub>2</sub>, N-Ru/RuO<sub>2</sub>, N-RuO<sub>2</sub>/NiO, Ru/RuO<sub>2</sub>/NiO, and N-Ru/RuO<sub>2</sub>/NiO, respectively.

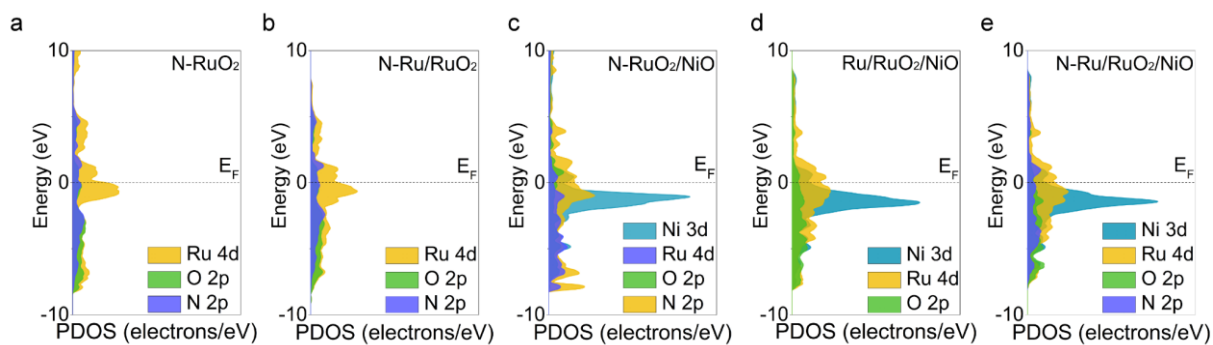


**Fig. S52.** Density of states (DOS) for (a) N-RuO<sub>2</sub>, (b) N-Ru/RuO<sub>2</sub>, (c) N-RuO<sub>2</sub>/NiO, (d) Ru/RuO<sub>2</sub>/NiO, and (e) N-Ru/RuO<sub>2</sub>/NiO.

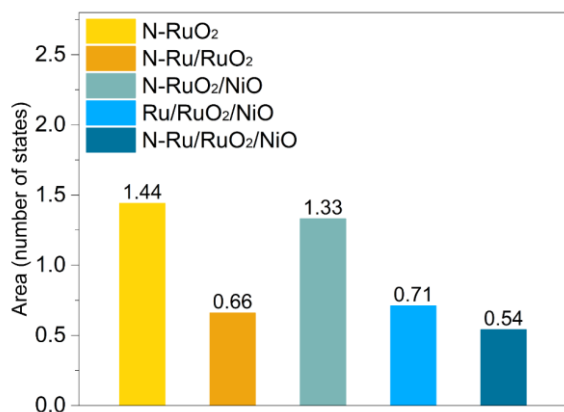


**Fig. S53.** Integration areas of Ru orbital and O orbital of water below Fermi level (calculated from Fig. 6d–6h).

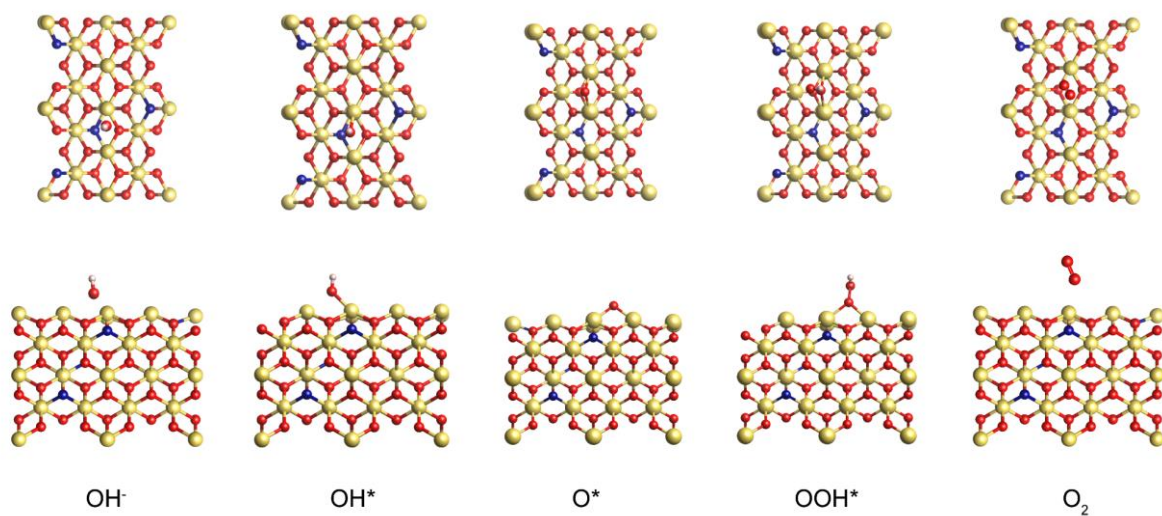


**Fig. S54.** Corresponding atomic structures of N-RuO<sub>2</sub> for the reaction pathway in OER. The yellow, dark blue, red and pink balls represent Ru, N, O and H atoms, respectively.

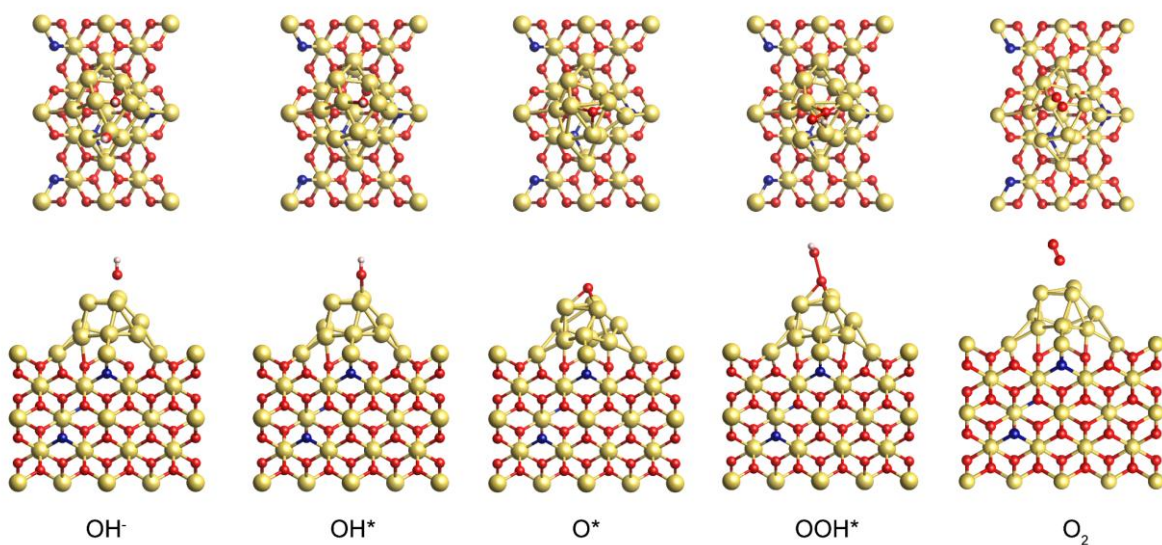


**Fig. S55.** Corresponding atomic structures of N-Ru/RuO<sub>2</sub> for the reaction pathway in OER. The yellow, dark blue, red and pink balls represent Ru, N, O and H atoms, respectively.

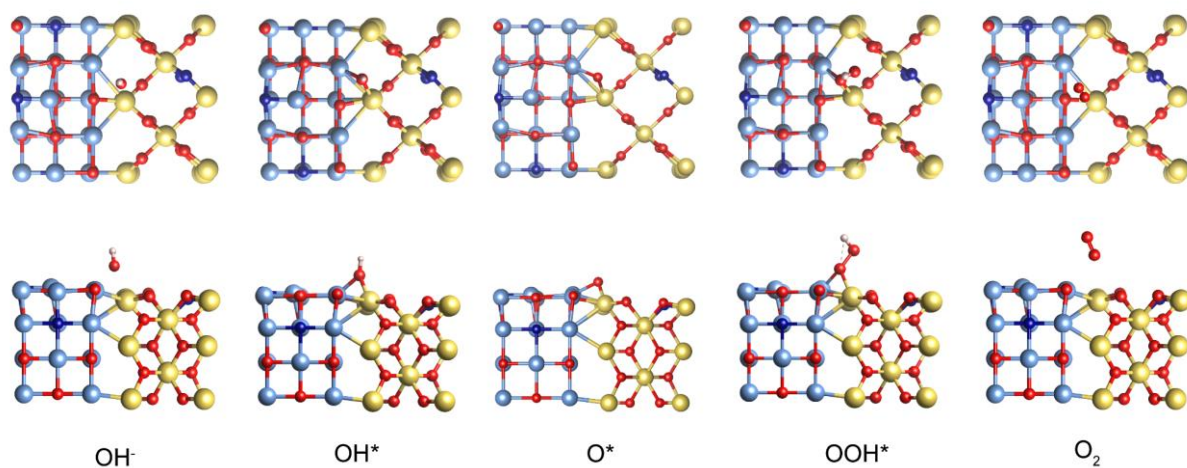


**Fig. S56.** Corresponding atomic structures of N-RuO<sub>2</sub>/NiO for the reaction pathway in OER. The yellow, blue, dark blue, red and pink balls represent Ru, Ni, N, O and H atoms, respectively.

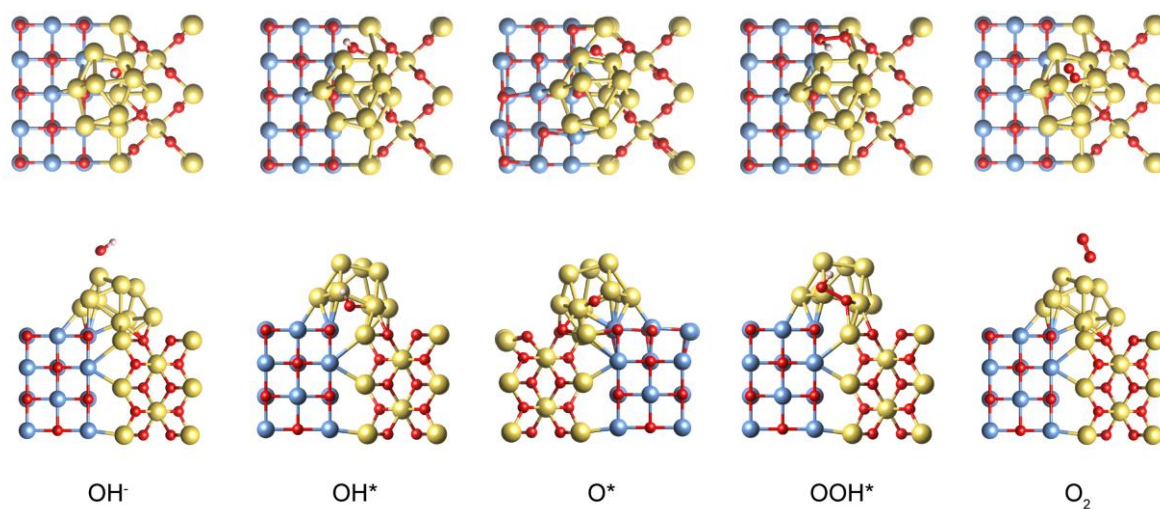


**Fig. S57.** Corresponding atomic structures of Ru/RuO<sub>2</sub>/NiO for the reaction pathway in OER. The yellow, blue, red and pink balls represent Ru, Ni, O and H atoms, respectively.

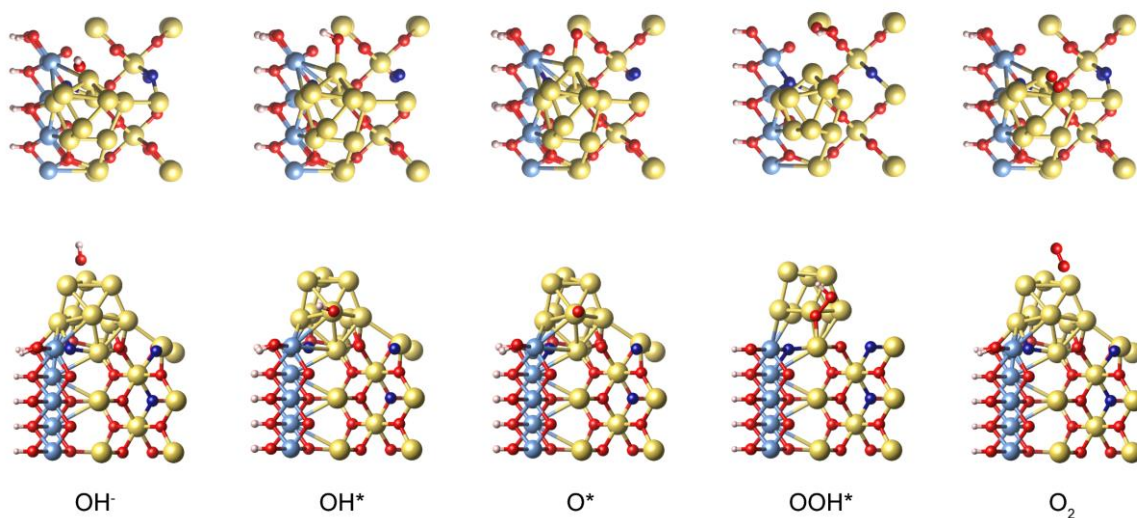


**Fig. S58.** Corresponding atomic structures of N-Ru/RuO<sub>2</sub>/NiO for the reaction pathway in OER. The yellow, blue, dark blue, red and pink balls represent Ru, Ni, N, O and H atoms, respectively.

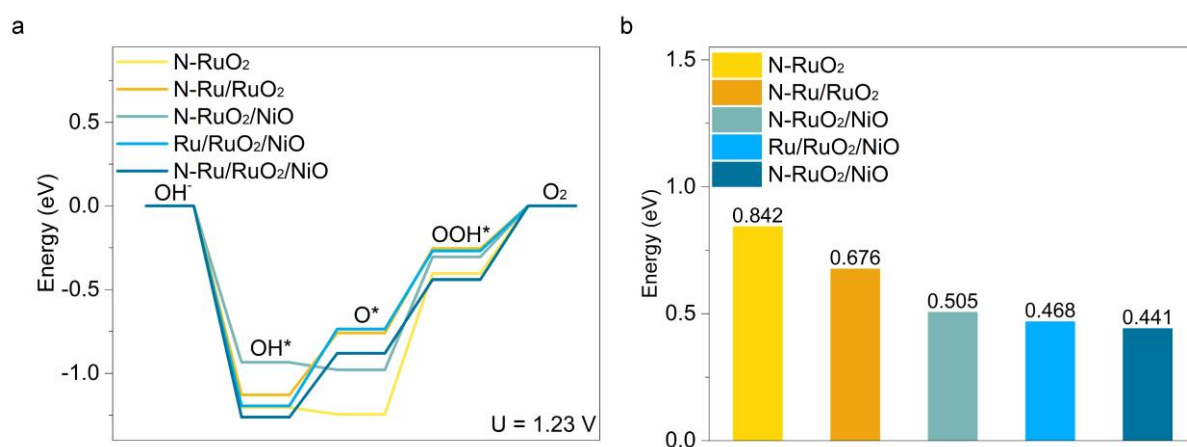


**Fig. S59.** (a) Energetic pathway for OER in an alkaline environment under  $U = 1.23$  V (b) Overpotential of the rate-determining step in OER under  $U = 1.23$  V for N-RuO<sub>2</sub>, N-Ru/RuO<sub>2</sub>, N-RuO<sub>2</sub>/NiO, Ru/RuO<sub>2</sub>/NiO, N-Ru/RuO<sub>2</sub>/NiO, respectively.

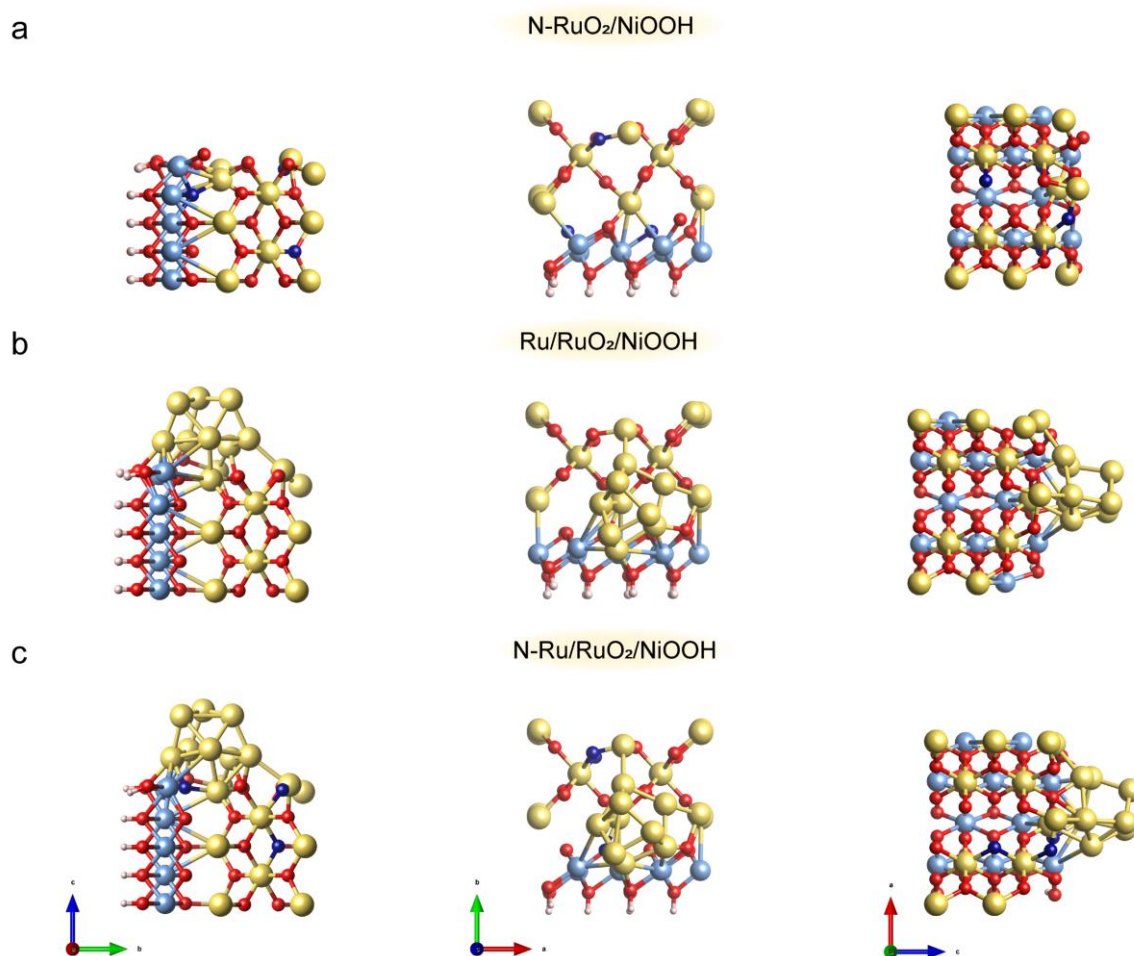


**Fig. S60.** Optimized atomic configurations of (a) nitrogen-doped RuO<sub>2</sub>/NiOOH (N-RuO<sub>2</sub>/NiOOH), (b) Ru/RuO<sub>2</sub>/NiOOH, and (c) nitrogen-doped Ru/RuO<sub>2</sub>/NiOOH (N-Ru/RuO<sub>2</sub>/NiOOH) composite models under different viewpoints. The yellow, blue, dark blue, red and pink balls represent Ru, Ni, N, O and H atoms, respectively.

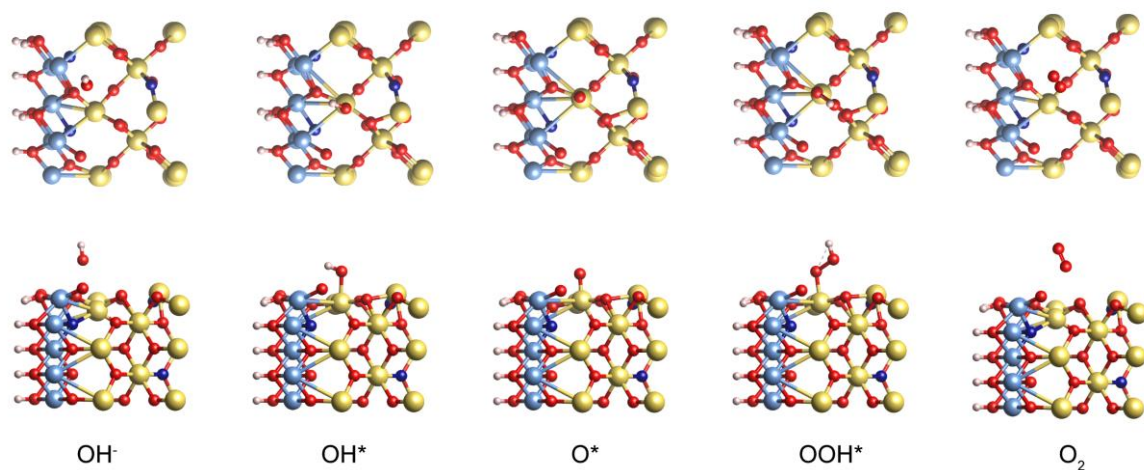


**Fig. S61.** Corresponding atomic structures of N-RuO<sub>2</sub>/NiOOH for the reaction pathway in OER. The yellow, blue, dark blue, red and pink balls represent Ru, Ni, N, O and H atoms, respectively.

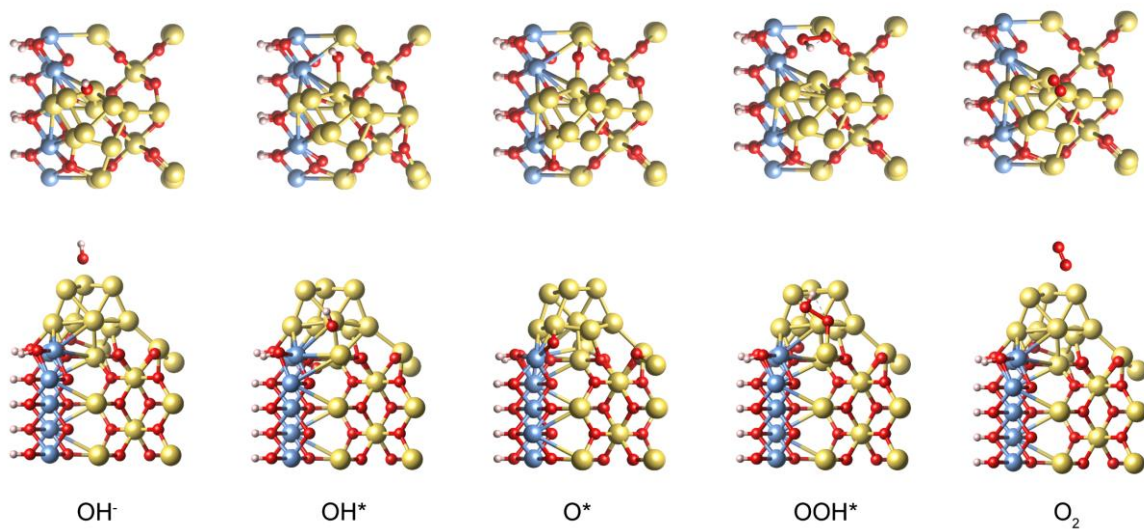


**Fig. S62.** Corresponding atomic structures of Ru/RuO<sub>2</sub>/NiOOH for the reaction pathway in OER. The yellow, blue, dark blue, red and pink balls represent Ru, Ni, O and H atoms, respectively.

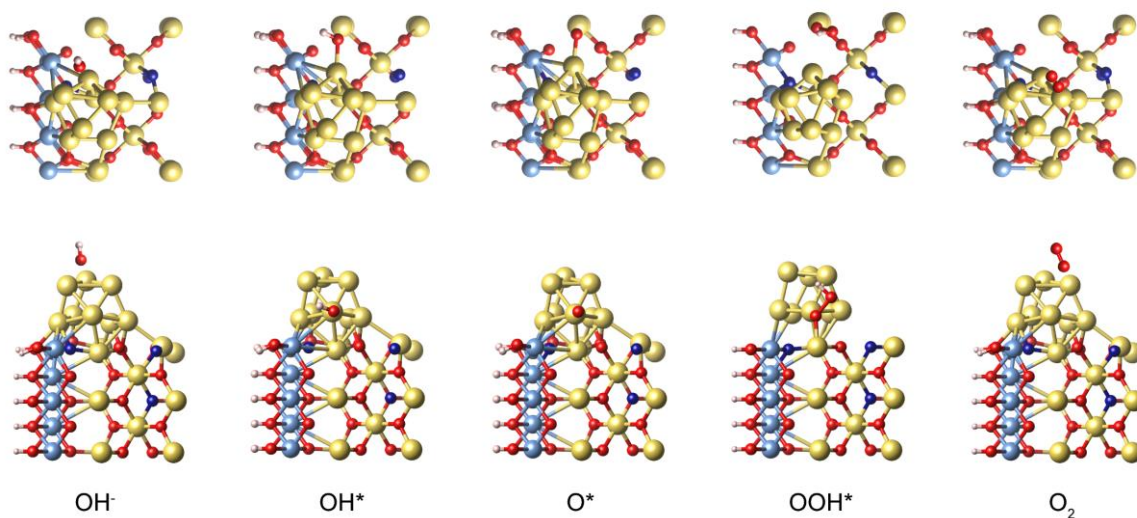


**Fig. S63.** Corresponding atomic structures of N-Ru/RuO<sub>2</sub>/NiOOH for the reaction pathway in OER. The yellow, blue, dark blue, red and pink balls represent Ru, Ni, N, O and H atoms, respectively.

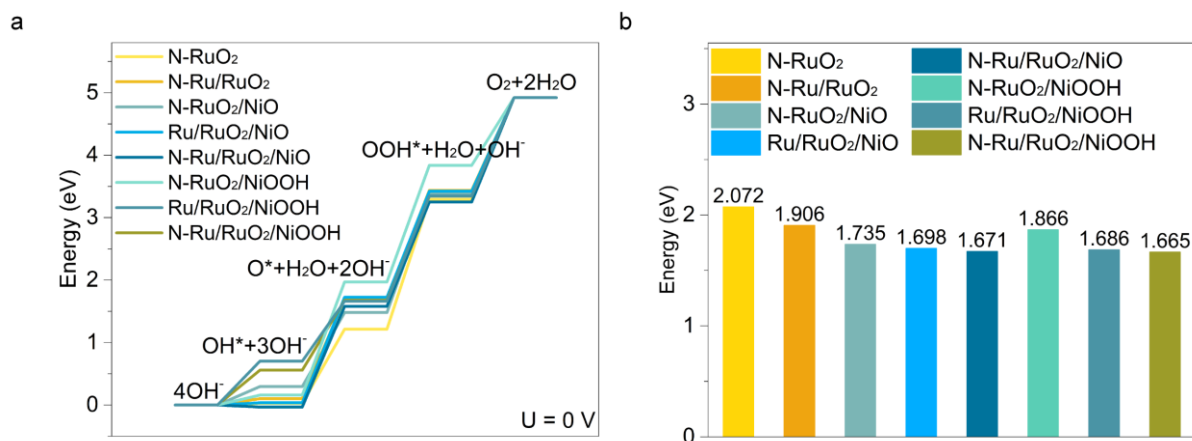


**Fig. S64.** (a) Energetic pathway for OER in an alkaline environment under  $U = 0$  V, and (b) overpotential of the rate-determining step in OER under  $U = 0$  V for N-RuO<sub>2</sub>, N-Ru/RuO<sub>2</sub>, N-RuO<sub>2</sub>/NiO, Ru/RuO<sub>2</sub>/NiO, N-Ru/RuO<sub>2</sub>/NiO, N-RuO<sub>2</sub>/NiOOH, Ru/RuO<sub>2</sub>/NiOOH and N-Ru/RuO<sub>2</sub>/NiOOH, respectively.

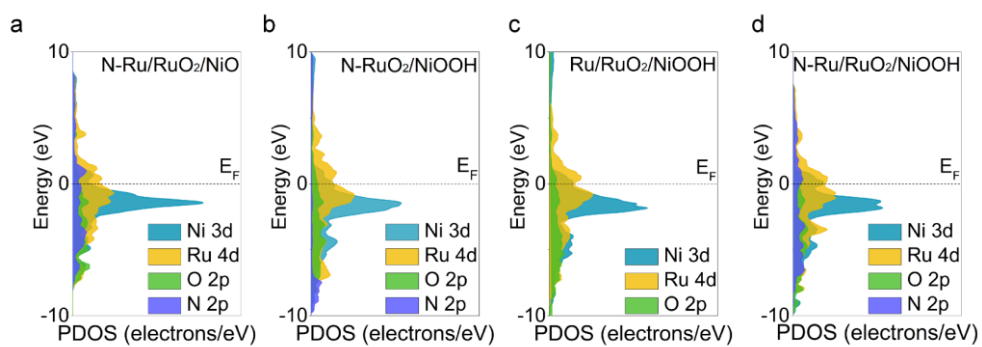


**Fig. S65.** DOS for (a) N-Ru/RuO<sub>2</sub>/NiO, (b) N- RuO<sub>2</sub>/NiOOH, (c) N-Ru/RuO<sub>2</sub>/NiOOH, and (d) N-Ru/RuO<sub>2</sub>/NiOOH.

## Supplementary Tables

**Table S1.** Comparison of recently reported representative electrocatalysts for HER in 1.0 M KOH.

Catalysts	Overpotential at 100 mA cm <sup>-2</sup> (mV)	Overpotential at 200 mA cm <sup>-2</sup> (mV)	Reference
Mesoporous composite film with cylindrical cavities on nickel foam	39	56	This work
Mesoporous composite film with spherical cavities on nickel foam	57	78	This work
(Ru-Co)O <sub>x</sub> /CC	89	~150	10
Ir@Ni-NDC	74	119	11
Ru/Ni <sub>3</sub> V-LDH	~62	90	12
Ru-NiSe <sub>2</sub> /NF	~100		13
Co-ZnRuO <sub>x</sub>	~80	~100	14
RuO <sub>2</sub> /NiO/NF	100		15
NiFeRu-LDH/NF	120		16
Ru/Cu-RuO <sub>2</sub> @C	142	~263	17
2% Ru-NCO	138	~175	18
Ni-Ru@Fe/C@CNT	110	149	19
Ru/Ni/WC@NPC	~120	~200	20
Ru-NiCoP/NF	103	~148	21
Ru <sub>1</sub> /D-NiFe LDH	61	~85	22

**Table S2.** Comparison of recently reported representative electrocatalysts for OER in 1.0 M KOH.

<b>Catalysts</b>	<b>Overpotential at 200 mA cm<sup>-2</sup> (mV)</b>	<b>Tafel slope (mV dec<sup>-1</sup>)</b>	<b>Reference</b>
Mesoporous composite film with cylindrical cavities on nickel foam	70@250 mA cm <sup>-2</sup>	27.4	This work
Mesoporous composite film with spherical cavities on nickel foam	70	36.8	This work
Ru-NiCoP/NF	~310	84.5	21
(Ru-Ni)O <sub>x</sub>	~345	73.5	23
(Ru-Co)O <sub>x</sub> /CC	~270	60.8	10
Vs-Ru-Ni <sub>9</sub> S <sub>8</sub>	~250	77.6	24
Ir@Ni-NDC	~290	44.7	11
Ru/Ni <sub>3</sub> V-LDH	280	33.0	12
NiVRu-LDH	~395	83.0	25
Ru <sub>1</sub> /D-NiFe LDH	~230	31.0	22
Ru-NiSe <sub>2</sub> /NF	~290	60.5	13
Co-ZnRuO <sub>x</sub>	~390	67.6	14
NiFeRu-LDH/NF	~270	32.4	16
Ru/Cu-RuO <sub>2</sub> @C	~400	56.0	17
2% Ru-NCO	~290	59.0	18
Ni-Ru@Fe/C@CNT	287	31.0	19
Ni-Fe NP	~285	58.0	26

**Table S3.** Comparison of recently reported representative electrocatalysts for overall water splitting in 1.0 M KOH.

<b>Catalysts</b>	<b>Potential at 100 mA cm<sup>-2</sup>(V)</b>	<b>Potential at 200 mA cm<sup>-2</sup> (V)</b>	<b>Reference</b>
Mesoporous composite film with cylindrical cavities	1.470	1.530	This work
Mesoporous composite film with spherical cavities	1.510	1.590	This work
Ru-NiCoP/NF	1.716		21
(Ru-Ni)O <sub>x</sub>	1.700		23
(Ru-Co)O <sub>x</sub> /CC	1.617	~1.635	10
Vs-Ru-Ni <sub>9</sub> S <sub>8</sub>	~1.627	~1.670	24
Ir@Ni-NDC	1.630	1.700	11
Ru/Ni <sub>3</sub> V-LDH	1.630	1.710	12
NiVIr-LDH  NiVRu-LDH	~1.673		25
Ni-Fe NP	~1.750		26
Co-ZnRuO <sub>x</sub>	~1.630	~1.740	14
Ru/Co-N-C-800 °C	1.660		27
RFNOH-10	1.600	~1.650	28
NiFeRu-LDH/NF	~1.700		16
Ru/Cu-RuO <sub>2</sub> @C	1.670		17
2% Ru-NCO	~1.600	~1.650	18
Ni-Ru@Fe/C@CNT	1.770	1.960	19

## References

1. Y. Cui, H. Zhu, J. Cai and H. Qiu, *Nat. Commun.* 2021, **12**, 5682.
2. Kresse, G. and Furthmüller, J. *Phys. Rev. B* 1996, **54**, 11169–11186.
3. J. P. Perdew, K. Burke, M. Ernzerhof, *Phys. Rev. Lett.* 1996, **77**, 3865-3868.
4. G. Kresse, D. Joubert, *Phys. Rev. B* 1999, **59**, 1758-1775.
5. S. Grimme, J. Antony, S. Ehrlich, H. Krieg, *J. Chem. Phys.* 2010, **132**, 154104.
6. H. J. Monkhorst and J. D. Pack, *Phys. Rev. B*, 1976, **13**, 5188-5192.
7. K. Momma and F. Izumi, *J. Chem. Phys.*, 2011, **44**, 1272-1276.
8. Z. Wang, W. Xu, X. Chen, Y. Peng, Y. Song, C. Lv, H. Liu, J. Sun, D. Yuan, X. Li, X. Guo, D. Yang and L. Zhang, *Adv. Funct. Mater.*, 2019, **29**, 1902875.
9. P. C. Yu, X. L. Zhang, T. Y. Zhang, X. Y. Tao, Y. Yang, Y. H. Wang, S. C. Zhang, F. Y. Gao, Z. Z. Niu, M. H. Fan and M. R. Gao, *J. Am. Chem. Soc.*, 2024, **146**, 20379-20390.
10. C. Wang and L. Qi, *Angew. Chem. Int. Ed.*, 2020, **59**, 17219-17224.
11. J. Yang, Y. Shen, Y. Sun, J. Xian, Y. Long and G. Li, *Angew. Chem. Int. Ed.*, 2023, **62**, e202302220.
12. H. Sun, C. W. Tung, Y. Qiu, W. Zhang, Q. Wang, Z. Li, J. Tang, H. C. Chen, C. Wang and H. M. Chen, *J. Am. Chem. Soc.*, 2022, **144**, 1174-1186.
13. R. Qin, P. Wang, Z. Li, J. Zhu, F. Cao, H. Xu, Q. Ma, J. Zhang, J. Yu and S. Mu, *Small*, 2022, **18**, e2105305.
14. D. Liu, Z. Wu, J. Liu, H. Gu, Y. Li, X. Li, S. Liu, S. Liu and J. Zhang, *Small*, 2023, **19**, e2207235.
15. J. Liu, Y. Zheng, Y. Jiao, Z. Wang, Z. Lu, A. Vasileff and S. Z. Qiao, *Small*, 2018, **14**, e1704073.
16. G. Chen, T. Wang, J. Zhang, P. Liu, H. Sun, X. Zhuang, M. Chen and X. Feng, *Adv. Mater.*, 2018, **30**, 1706279.
17. K. Yang, P. Xu, Z. Lin, Y. Yang, P. Jiang, C. Wang, S. Liu, S. Gong, L. Hu and Q. Chen, *Small*, 2018, **14**, e1803009.
18. J. Zhang, J. Lian, Q. Jiang and G. Wang, *Chem. Eng. J.*, 2022, **439**, 135634.
19. T. Gao, X. Li, X. Chen, C. Zhou, Q. Yue, H. Yuan and D. Xiao, *Chem. Eng. J.*, 2021, **424**, 130416.

20. A. Salah, L. Zhang, H. Tan, F. Yu, Z. Lang, N. Al - Ansi and Y. Li, *Adv. Energy Mater.*, 2022, **12**, 2200332.
21. D. Chen, R. Lu, Z. Pu, J. Zhu, H.-W. Li, F. Liu, S. Hu, X. Luo, J. Wu, Y. Zhao and S. Mu, *Appl. Catal. B: Environ.*, 2020, **279**, 119396.
22. P. Zhai, M. Xia, Y. Wu, G. Zhang, J. Gao, B. Zhang, S. Cao, Y. Zhang, Z. Li, Z. Fan, C. Wang, X. Zhang, J. T. Miller, L. Sun and J. Hou, *Nat. Commun.*, 2021, **12**, 4587.
23. H. Zhang, Y. Lv, C. Chen, C. Lv, X. Wu, J. Guo and D. Jia, *Appl. Catal. B: Environ.*, 2021, **298**, 120611.
24. Q. Gao, W. Luo, X. Ma, Z. Ma, S. Li, F. Gou, W. Shen, Y. Jiang, R. He and M. Li, *Appl. Catal. B: Environ.*, 2022, **310**, 121356.
25. D. Wang, Q. Li, C. Han, Q. Lu, Z. Xing and X. Yang, *Nat. Commun.*, 2019, **10**, 3899.
26. B. H. R. Suryanto, Y. Wang, R. K. Hocking, W. Adamson and C. Zhao, *Nat. Commun.*, 2019, **10**, 5599.
27. C. Rong, X. Shen, Y. Wang, L. Thomsen, T. Zhao, Y. Li, X. Lu, R. Amal and C. Zhao, *Adv. Mater.*, 2022, **34**, e2110103.
28. X. Xiao, X. Wang, X. Jiang, S. Song, D. Huang, L. Yu, Y. Zhang, S. Chen, M. Wang, Y. Shen and Z. Ren, *Small Methods*, 2020, **4**, 1900796.